AGU PUBLICATIONS

JGR

Journal of Geophysical Research: Space Physics

RESEARCH ARTICLE

10.1002/2014JA020280

Key Points:
- The dissipation of GWs creates global changes to the thermosphere and ionosphere

Supporting Information:
- Readme
- Movie S1
- Movie S2

Correspondence to:
S. L. Vadas,
vasha@cora.nwra.com

Citation:
Vadas, S. L., H.-L. Liu, and R. S. Lieberman (2014), Numerical modeling of the global changes to the thermosphere and ionosphere from the dissipation of gravity waves from deep convection, *J. Geophys. Res. Space Physics*, *119*, doi:10.1002/2014JA020280.

Received 13 JUN 2014
Accepted 27 JUL 2014
Accepted article online 4 AUG 2014

Numerical modeling of the global changes to the thermosphere and ionosphere from the dissipation of gravity waves from deep convection

S. L. Vadas[1], H.-L. Liu[2], and R. S. Lieberman[3]

[1]NWRA/CoRA Office, Boulder, Colorado, USA, [2]National Center for Atmospheric Research (HAO/NCAR), Boulder, Colorado, USA, [3]GATS-Inc., Boulder, Colorado, USA

Abstract During the minimum of solar cycles 23–24, the Sun was extremely quiet; however, tropospheric deep convection was strong and active. In this paper, we model the gravity waves (GWs) excited by deep convective plumes globally during 15–27 June in 2009 and in 2000 (previous solar maximum). We ray trace the GWs into the thermosphere and calculate the body force/heatings which result where they dissipate. We input these force/heatings into a global dynamical model and study the neutral and plasma changes that result. The body forces induce horizontal wind (u'_H) and temperature (T') perturbations, while the heatings primarily induce T'. We find that the forces create much larger T' than the heatings. u'_H consists of clockwise and counterclockwise circulations and "jet"-like winds that are highly correlated with deep convection, with $|u'_H| \sim 50$–200 m/s. u'_H and T' are much larger during 2009 than 2000. u'_H decreases slightly (significantly) with altitude from $z \sim 150$ to 400 km during 2009 (2000). T' perturbations at $z = 350$ km primarily propagate westward at ~460 m/s, consistent with migrating tides. It was found that planetary-scale diurnal and semidiurnal tides are generated in situ in the thermosphere, with amplitudes ~10–40 m/s at $z = 250$ km. The largest-amplitude in situ tides are DW1, D0, DW2, SW2, SW3, and SW5. Smaller-amplitude in situ tides are S0, SE2, and SW3. Total electron content (TEC′) perturbations of 1–2.5 (2–3.5) total electron content units (TECU, where 1 TECU = 10^{16} el m^{-2}) during 2009 (2000) are created in the upper atmosphere above nearby regions of deep tropical convection. For a given local time (LT), there are 2 to 3 TEC′ peaks in longitude around the Earth.

1. Introduction

It is widely believed that gravity waves (GWs) play a significant role in the transport of energy and momentum from the lower atmosphere to the mesosphere. GWs are created when stable fluid is disturbed, such as occurs when a convective plume overshoots the tropopause into the stratosphere. As these GWs propagate upward into changing wind and temperature environments, their intrinsic properties change, and their amplitudes grow exponentially with altitude. Many GWs with large amplitudes and small vertical wavelengths λ_z break by the time they reach the mesopause [e.g., *Fritts and Alexander*, 2003]. The resulting momentum flux divergences are highly intermittent and variable [*Yamada et al.*, 2001; *Hecht et al.*, 1997; *Fritts et al.*, 2002, 2006; *Vadas et al.*, 2003]. Such divergences reverse the wind near the mesopause and drives the upper mesosphere away from radiative equilibrium [e.g., *Fritts and Alexander*, 2003].

Recently, studies have begun to illuminate the dynamical role that GWs from deep convection and other lower atmospheric sources have on the thermosphere and ionosphere when they dissipate. Because most GWs from the lower atmosphere dissipate below $z \sim 300$ km [*Vadas*, 2007; *Fritts and Vadas*, 2008], the dynamical forcing they provide occurs primarily below $z \sim 300$ km [*Vadas and Fritts*, 2004, 2006; *Miyoshi and Fujiwara*, 2008; *Yiğit et al.*, 2009]. It is now known that the dissipation of GWs from single and multiple deep convective plumes, clusters, and complexes (1) accelerates the neutral, horizontal wind by ~0.2–1.0 m/s^2 at $z \sim 120$–250 km over spatially localized regions of ~100 – 800 km and time scales of ~10–15 min; (2) creates spatially and temporally localized neutral horizontal wind perturbations of ~50–200 m/s that decay from viscosity in time; and (3) excites a rich spectrum of upward and downward propagating secondary GWs that have horizontal wavelengths of $\lambda_H \sim 100 - 4000$ km and phase speeds of $c_H \sim 100$–500 m/s [*Vadas and Liu*, 2009, 2013; *Vadas and Crowley*, 2010; *Vadas*, 2013]. Note that the GWs create moving plasma

perturbations known as traveling ionospheric disturbances. Those secondary GWs having large scales propagate globally and reach vertical heights of at least $z \geq 400$ km [*Vadas and Liu*, 2013; *Liu and Vadas*, 2013]. Other studies using a parameterized orographic GW spectrum show that dissipating GWs change the zonal mean zonal winds on a global scale up to $z \sim 240$ km with accelerations as large as ~150m/s/d [*Yiğit et al.*, 2009] and create zonal wind variability in the thermosphere of ~100–200 m/s [*Miyoshi and Fujiwara*, 2008]. Thus, GWs transfer significant amounts of momentum from the lower atmosphere to the thermosphere and ionosphere.

Additionally, heating and cooling also accompanies GW dissipation [*Walterscheid*, 1981; *Liu*, 2000; *Becker*, 2004]. In the thermosphere, such dissipative processes yield temperature changes of ~100 K using a parameterized orographic GW spectrum [*Yiğit and Medvedev*, 2009]. Employing a single convective plume and idealized temperature and wind profiles, the heat/cooling rates were shown to be ~0.06 to 0.15 K/s and consisted of hotter/colder dipoles at z ~150–200 km, and a heating at $z \sim 240$–260 km [*Vadas*, 2013].

Although GWs from many lower atmospheric sources dissipate in the thermosphere, deep convection is an intermittent, common, and strong source of lower atmospheric, large-λ_z, high-frequency GWs (1) near the equator year round and (2) at midlatitudes in the spring, summer, and fall. Those having large λ_z and c_H can propagate readily into the thermosphere [*Vadas*, 2007]. Additionally, deep convection is the most important source of lower atmospheric GWs near the equator.

Although many of the local dynamical changes to the thermosphere and ionosphere due to the dissipation of GWs from deep convection within specific regions (such as Brazil) are known, no study to date has examined the global impacts on the dynamics of the thermosphere and ionosphere from nonparameterized deep convection globally. Furthermore, no study has examined the dependence of the response on the solar cycle. Several studies have shown that the momentum flux divergence caused by the dissipation of GWs from a single deep convective plume was 2–3 times larger during extreme solar minimum (i.e., thermospheric temperature of $\overline{T} \sim 600$ K) than during solar maximum (i.e., $\overline{T}$~1200–1500 K) [*Vadas and Fritts*, 2006; *Vadas*, 2013]. Therefore, it is likely that the neutral horizontal wind perturbations and secondary GW amplitudes created from deep convection during extreme solar minimum are larger than during solar maximum. A confirmation of this effect is important for increasing our understanding of the effect deep convection has on the thermosphere and ionosphere.

During the recent solar minimum between cycles 23 and 24 (i.e., from 2007 to 2010), the Sun was extremely quiet, and the thermospheric density and temperature were quite low (i.e., exhibited extreme solar minimum) [*Araujo-Pradere et al.*, 2011; *Emmert et al.*, 2010; *Haaser et al.*, 2010]. However, as we will see in this paper, deep convection (created by solar heating near the Earth's surface) was strong and energetic as compared to during the previous solar maximum. The purpose of this paper is to investigate, for the first time, the global neutral and plasma changes that occurred in the thermosphere and ionosphere during (1) the minimum of cycles 23–24 and (2) the maximum of cycle 23 that result from the dissipation of realistically modeled GWs excited from intermittent, highly localized, deep convective plumes. We choose the study period to be 15–27 June, which is 13 consecutive days during the Northern Hemisphere summer. We choose two study years. The first study year we choose is 2009, when the number of sunspots was extremely low during 15–27 June. The second study year we choose is 2000, when the number of sunspots was close to maximum during the previous solar maximum (R.A.M. Van der Linden and the SIDC team, online catalogue of the sunspot index, http://sidc.oma.be/html/sunspot.html). For this study, we locate the overshooting convective plumes from IR satellite images that span the Earth.

This study utilizes three numerical models. The first is a convective plume envelope model, which calculates the analytic Fourier-Laplace GW solutions to an updraft of fluid near the tropopause (i.e., primary GW spectra) [*Vadas and Fritts*, 2009; *Vadas*, 2013]. The second is a dissipative GW ray trace model, which ray traces the individual primary GWs (with their phases) into the thermosphere, and calculates the force/heatings that occur where they dissipate [*Vadas and Fritts*, 2009; *Vadas*, 2013]. The third is the high-resolution thermosphere-ionosphere-mesosphere-electrodynamics general circulation model (TIME-GCM), which calculates the global changes to the thermosphere and ionosphere as a result of the inputted (spatially and temporally varying) force/heatings [*Roble and Ridley*, 1994]. The TIME-GCM is an upper atmosphere model based on the primitive equations. The main purpose of the first two models is to calculate realistic subgrid-scale force/heatings associated with the dissipation of convective GWs in order to input them into the TIME-GCM, since the TIME-GCM cannot resolve the primary convective GWs directly.

(The high-resolution TIME-GCM can only resolve GWs with $\lambda_H \geq 2000$ km due to added grid-scale numerical dissipation [*Vadas and Liu*, 2009]).

In section 2, we review our convective plume model and describe the data sets we utilize to determine the convective plume parameters. Section 3 describes our new global ray trace model and shows how we calculate the body force/heatings where the primary GWs dissipate. In section 4, we show the global responses which occur in the thermosphere and ionosphere as a result of these convectively generated force/heatings. Section 5 contains a discussion and our conclusions.

2. GW Convective Plume Model and Convective Plume Data

In this section, we describe the model we use to calculate the primary GWs excited by a convective plume/object. We discuss the data sets we use to extract the necessary convective plume parameters. We then show the distributions of deep convective plumes during the study periods in 2009 and 2000.

2.1. Excitation of Primary GWs Using a Convective Plume Envelope Model

Over the past few decades, many numerical models have been developed to simulate the GWs excited by deep convection [e.g., *Holton and Alexander*, 1999; *Pandya and Alexander*, 1999; *Horinouchi et al.*, 2002; *Lane et al.*, 2003]. Within a moist convective system, both diabatic forcing (i.e., latent heating and cooling) and nonlinear forcing excite GWs [*Lane et al.*, 2001]. Since these sources are largely out of phase with one another, linear dry GW excitation models which include only one of these sources must reduce the excited GW amplitudes by a factor of 2 and must only include GWs with horizontal phase speeds $c_H > 20$–25 m/s [*Song et al.*, 2003; *Choi et al.*, 2007]. Currently, there are linear, "dry-air" GW excitation models which implement (1) diabatic forcing [*Alexander et al.*, 1995; *Piani et al.*, 2000; *Walterscheid et al.*, 2001; *Beres*, 2004] and (2) convective overshoot [*Stull*, 1976; *Vadas and Fritts*, 2009]. GW excitation from deep convection excites high-frequency GWs with $\lambda_H \sim 1$ km to hundreds of kilometers, and with periods of 5 min to a few hours.

Our convective plume model is an idealized, linear model which implements the latter process [*Vadas and Fritts*, 2009; *Vadas et al.*, 2009, 2012]; it models the envelope of a 3-D convective plume as a Gaussian, vertical body force (plus its identical mirror image below the Earth's surface), thereby neglecting the small-scale processes which create small-scale GWs. Since very small scale GWs cannot propagate above the stratopause, this model is appropriate for mesospheric and thermospheric GW studies for GWs with phase speeds of $c_H > 20$ m/s. This model is not a direct numerical simulation; instead, it uses analytic, Fourier-Laplace compressible solutions to determine the excited, linear, GW spectrum as a function of wave vector (k, l, m) [*Vadas*, 2013]. Each convective plume is specified by the force's full diameter $\mathcal{D}_H$, full depth $\mathcal{D}_z$, updraft velocity $w_{\rm pl}$, longitude, latitude, height (1–2 km above the tropopause altitude), and time.

Additionally, each plume is specified as being "single", part of a "cluster", or part of a "complex." We utilize the term "convective object" to denote a single plume, a cluster, or a complex. On average, a cluster consists of three noninteracting plumes which form an equilateral triangle. Based on the average distance seen in the satellite images, we set the separation distance between the corners of the triangle (i.e., between the plume centers) to be $3.0\mathcal{D}_H$. On average, a complex consists of three interacting plumes which form a tighter equilateral triangle. Based on the average distance seen in the satellite images, we set the separation distance between the corners of the triangle (i.e., between the plume centers) to be $2.25\mathcal{D}_H$. (Note that these definitions are different from those in *Vadas and Liu* [2013]).

The grid spacings for calculating the Fourier-Laplace solutions are $\Delta_x = \Delta_y = (\mathcal{D}_H/2.25)$ in the x and y directions, and $\Delta_z = (\mathcal{D}_z/2.25)$ in the z direction. Thus, each plume is modeled by ~11 grid points. We then take the Fourier transform of the Gaussian vertical body force(s) (and its image(s)) and compute the analytic GW solutions as a function of wave vector when the force(s) is finished. Note that only those excited GWs with $\lambda_i \geq 2\Delta_i$ can be computed [*Vadas and Fritts*, 2009]. These Fourier-Laplace compressible solutions contain the amplitudes and phases of the primary GWs excited by this idealized convective object.

2.2. Data Used as Input to the Convective Plume Model

The convective plumes during 15–27 June 2009 were identified worldwide (180°W to 180°E and 90°S to 90°N) using the infrared (IR) full-disk images from the following weather satellites: GOES (GOES11 and GOES12), European Organisation for the Exploitation of Meteorological Satellites (EUMETSAT) Meteosat (M7 and M9), and Joint Space Operations Center Mission System (JMS) (MTS) (available at www.class.ncdc.noaa.gov). All satellites are located above the equator (0° latitude) in geostationary orbits.

Table 1. Longitude Ranges for Identifying Plumes From Satellite Images

Year	Satellite	Longitude Range	IR Band (μm)	Pixel Resolution (km)
2009	GOES11	165°W to 120°W	10.2–11.2	4
2009	GOES12	120°W to 30°W	10.2–11.2	4
2009	M9	30°W to 15°E	10.5–12.5	5
2009	M7	15°E to 105°E	10.6–12.5	5
2009	MTS	105°E to 180°E and 180°W to 165°W	10.3-11.3	4
2000	GOES10	180°W to 120°W	10.3–11.0	4
2000	GOES8	120°W to 30°W	10.2–11.2	4
2000	M7	30°W to 30°E	10.6–12.5	5
2000	M5	30°E to 90°E	10.6–11.8	5
2000	GMS5	90°E to 180°E	10.2–11.4	5

The GOES satellites cover North and South America, western Atlantic Ocean, and eastern Pacific Ocean. The EUMETSAT satellites cover the eastern Atlantic Ocean, Africa, Europe, western Asia, and Indian Ocean. The JMS satellite covers eastern Asia, Australia, and western Pacific Ocean. There are a few missing or dark images from which plumes could not be identified. They are GOES11 on 16 June at 9:00 UT and GOES12 on 23 June at 3:00 UT. The convective plumes during 15–27 June 2000 were identified using IR full-disk images from GOES8, GOES10, M5, M7, and Geostationary Meteorological Satellite GMS5. The missing or dark images in 2000 are GOES10 on 24 June at 6:00 UT and 9:00 UT, and 26 June at 21:00 UT. All of these satellites scanned the full-disk every 3 h. In Table 1, we list the longitude range we use, IR band and pixel resolution for each satellite. Note that the pixel sizes on the IR images are 4–5 km, which imply horizontal error bars (for determining the plume diameters and locations) of $\pm$(2–2.5) km. From these data sets, we obtain the convective object locations worldwide every 3 h. Note that because the actual longitude ranges of the satellites overlapped one another, we were able to avoid using the edges of the satellite images to identify the convective objects, thus minimizing the under and over representation of the identified convective objects.

As an example, Figure 1 shows a MTS IR image on 18 June 2009 at 23:32 UT. This image is hand marked by a meteorologist to identify the overshooting convective objects. Localized cold temperatures on the anvils imply convective overshoot, because a parcel of air which moves adiabatically through the tropopause and into the stratosphere has a colder temperature than the surrounding air [*Cotton and Anthes*, 1989]. However, some cold spots in the IR images may be bad data points, etc., so each cold spot must be examined carefully in order to determine if it displays convective overshoot. In this image, 64 convective objects are identified as overshooting the tropopause. Typically, 50 to 90 convective objects are identified per image. The minimum and maximum number of convective objects globally at a given UT are 155 and 328 in year 2009 and 205 and 327 in year 2000. The average number of plumes per UT is 244 in year 2009 and 276 in year 2000. Thus, deep convection was quite strong globally during our study periods in years 2009 and 2000. Note that convection is not just a function of solar irradiance; it also depends on moisture, sea surface temperature, etc.

For each identified convective object, its location, type (i.e., single plume, cluster, or complex), and plume diameter (from 5 to 30 km) are estimated and are recorded in a file. (Although determination of the diameters of the 5 km plumes is more error prone because of the satellite pixel sizes, the GWs excited from these small plumes do not play a significant role in the thermosphere because they have small λ_H and frequencies $\sim$ buoyancy frequency, thereby causing them to dissipate or reflect in the lower thermosphere). The average plume updraft velocity within an object, w_{pl}, is estimated from the convective available potential energy (CAPE) [*Vadas et al.*, 2012] and the overshoot altitude is estimated from the tropopause altitude (Trop height). The CAPE and Trop height are determined from the Global Forecast System Final Analyses, available every 6 h on a 1° $\times$ 1° latitude/longitude grid. Observations of the standard meteorological variables (wind, temperature, pressure, moisture, etc.) from surface, balloon, buoy, satellite, radar, and other observing systems are used in these analyses. Only those plumes with the arbitrary cutoff of $w_{pl} \geq 10$ m/s are recorded and utilized in this study. Such a cutoff is implemented because the resulting thermospheric force/heat/cooling amplitude is proportional to w_{pl}^2; thus, primary GWs excited by plumes

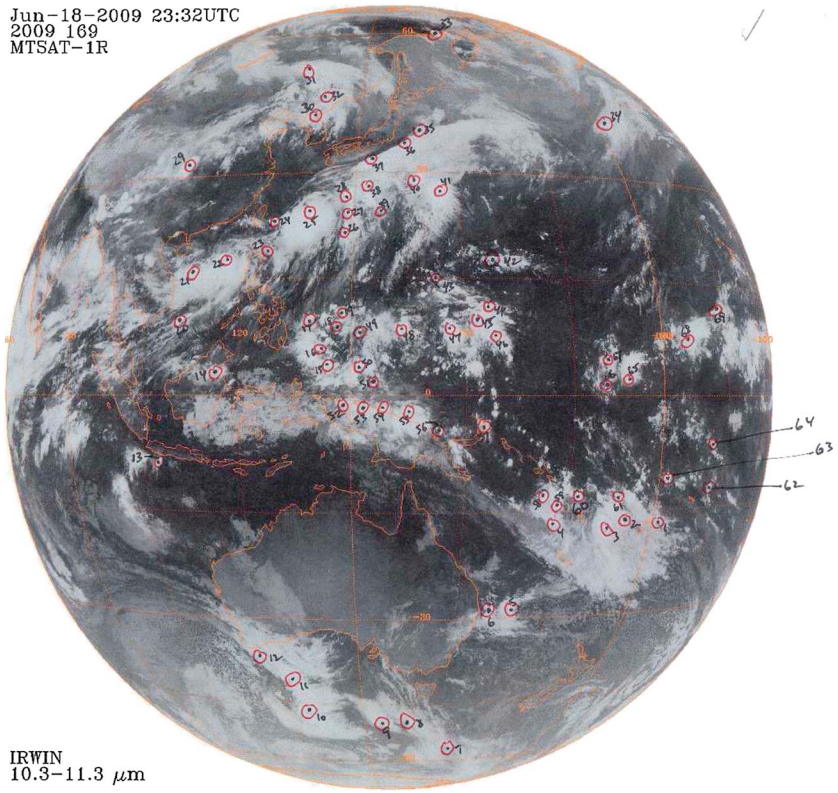

Figure 1. MTS IR satellite image at 23:32 UT on 18 June 2009 showing the Indonesian/Australian sector. Black dots surrounded by hand-drawn red circles indicate locations where convective overshoot (of the tropopause) occurred.

with $w_{pl} < 10$ m/s are not expected to play a significant role in forcing the thermosphere when and where they dissipate.

Figures 2a, 2c, 2e, 2g, and 2i show the total number of convective objects in 2009 in 10° longitude bins (summed in latitude) as a function of longitude. Although there is substantial daily variability, there are approximately ~5 convective hot spots which persist throughout the 13 day period, although these spots move somewhat and decrease/increase in intensity. These hot spots occur at 130–170°W (Pacific Ocean near Hawaii and Polynesian Islands), 60–90°W (Central, North, and South America), 0–30°W (western Africa), 60–100°E (India and the Indian Ocean), and 110–180°E (Indonesia, Philippine Islands, and western Pacific Ocean). We note that the number of plumes generally decreased in time over the Indian and Pacific Oceans over this 13 day period, suggesting that convection weakened there. Although the sea surface temperature (SST) was above 27.5°C (required for large-scale deep convection to occur), this is not a sufficient condition for deep convection to occur; convection is suppressed when there are regions of persistent divergent surface flow even when the SST is above 27.5°C [*Graham and Barnett*, 1987].

Figures 2b, 2d, 2f, 2h, and 2j show the average plume updraft velocity in each object, $\overline{w_{pl}}$. Typical values are $\overline{w_{pl}} \sim 20$–50 m/s. Figures 3 and 4 show the locations and times of the most energetic convective objects in 2009. Most of the convection occurs near the equator. While some of the convection occurs throughout the day (e.g., Central America), deep convection in Africa tends to occur at late UT.

Figure 5 shows the number of convective objects and $\overline{w_{pl}}$ in 2000. Four to five hot spots typically occur. The largest number of convective objects are located at 50–100°W (South and Central America), 30°W to 30°E (Africa), 60–100°E (India and Asia), and 100–170°E (Indonesia, Philippine Islands, and western Pacific Ocean). Typical updraft velocities are $\overline{w_{pl}} \sim 20$–50 m/s. Figures 6 and 7 show the locations and times of the most energetic convective objects in 2000. As in 2009, most of the convection occurs near the equator, with similar convective hot spots: in Central/northern South America, Africa, India/Indonesia/Philippines, and Pacific Ocean near Hawaii.

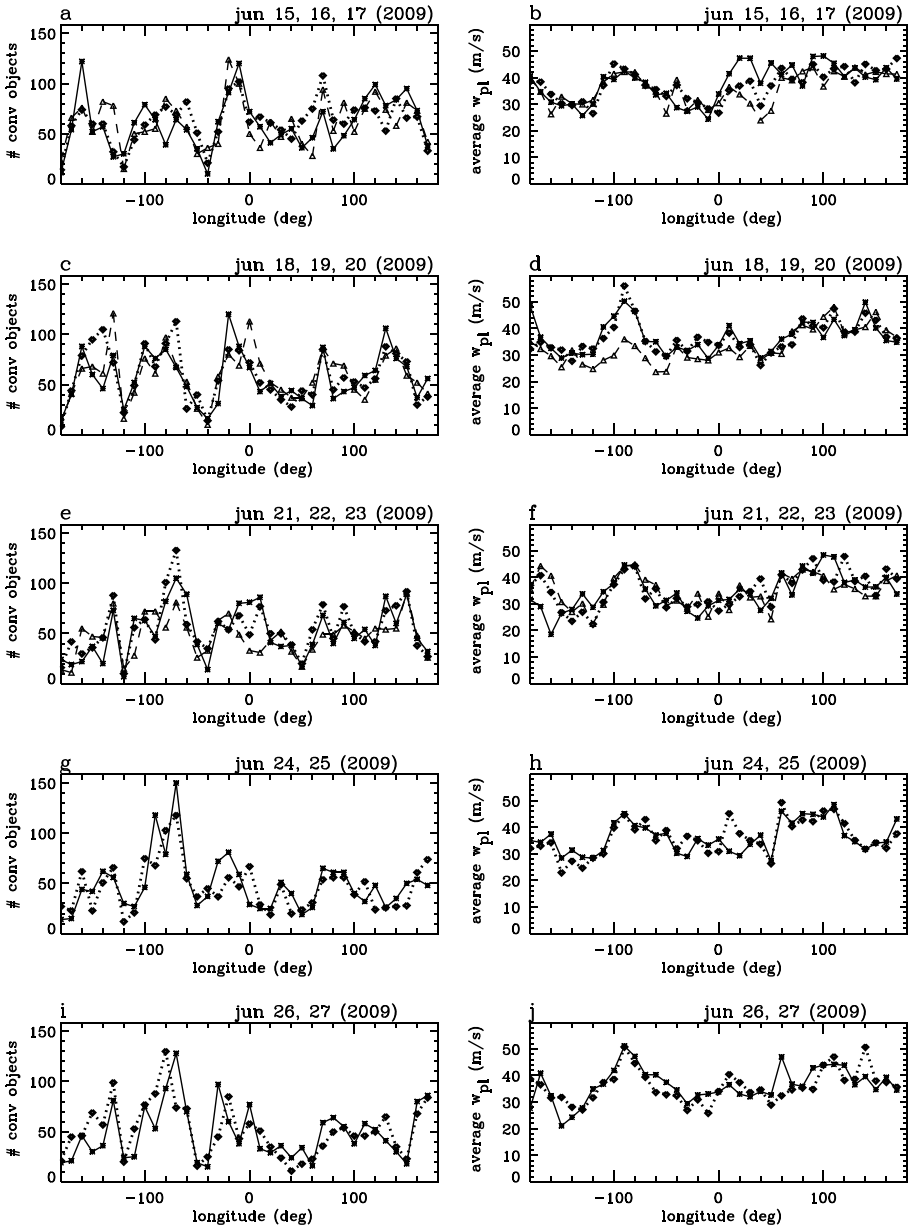

Figure 2. (a) The total number of plumes in 10° longitude bins for 15–17 June 2009 (solid, dotted, and dashed lines, respectively). (b) The average plume updraft velocities within these longitude bins for 15–17 June 2009 (solid, dotted, and dashed lines, respectively). (c, d) Same as Figures 2a and 2b but for 18–20 June 2009. (e, f) Same as Figures 2a and 2b but for 21–23 June 2009. (g, h) Same as Figures 2a and 2b but for 24–25 June 2009 (solid and dotted lines, respectively). (i, j) Same as Figures 2g and 2h but for 26–27 June 2009.

3. Ray Tracing and Calculation of Force/Heatings With New Global Model

In section 2, we reviewed the model we use to calculate the GWs excited by an overshooting convective object. In this section, we discuss the new global model we use to ray trace these GWs into the thermosphere, reconstruct the GW field, and calculate the thermospheric force/heat/coolings which result where they dissipate.

3.1. New Global Ray Trace Model With a High-Resolution Patch for Each Object

In order to propagate the primary convectively generated GWs into the thermosphere (with their phases), we utilize an anelastic, dissipative GW ray trace model [*Vadas and Fritts*, 2009; *Vadas et al.*, 2009, 2012; *Vadas and Liu*, 2013]. This model incorporates a GW dissipative dispersion relation which includes molecular

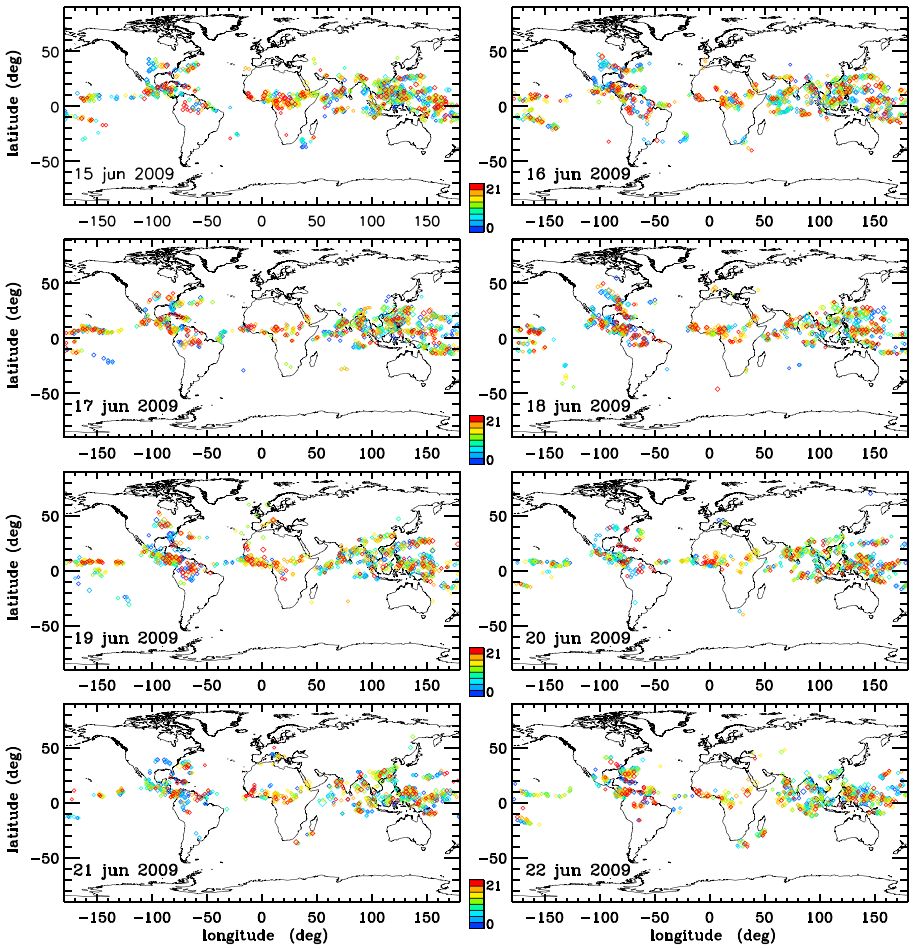

Figure 3. Deep convective objects identified as overshooting the tropopause for 15–22 June 2009. We only show those objects having the most energetic plumes with updraft velocities of $w_{pl} \geq 40$ m/s. A diamond denotes each object, with its size proportional to w_{pl}. The blue to red colors show 0, 3, 6, 9, 12, 15, 18, and 21 UT, respectively.

viscosity and thermal conductivity [*Vadas and Fritts*, 2005]. This dispersion relation neglects other forms of dissipation such as ion drag and wave-induced diffusion. Ion drag is unimportant for GWs with periods less than an hour during the daytime and less than a few hours during the nighttime [e.g., *Gossard and Hooke*, 1975], and wave-induced diffusion is likely not very important for GWs with periods less than an hour [*DelGenio and Schubert*, 1979]. This dispersion relation also neglects the Coriolis force, which is a good approximation for GWs with periods less than a few hours. Because most of the convectively generated GWs have periods less than an hour [e.g., *Lane et al.*, 2001] and because only those convectively generated GWs with periods much less than an hour are important for generating thermospheric body forces [e.g., *Vadas and Liu*, 2009], we can neglect ion drag, wave-induced diffusion, and the Coriolis force when ray tracing the primary GWs. Note that in the limit that GW dissipation is negligible, this relation reduces to the usual anelastic dispersion relation [*Eckermann and Marks*, 1996].

The ray trace model allows for the variation of the background wind, density, and temperature in space and time. Using the GW phases, the model reconstructs the GW field (i.e., the velocity, density, and temperature as a function of x, y, z, and t) in the mesosphere and thermosphere. Note that the reconstructed GW field at $z \sim 90$ km has been shown to agree very well with the exact solutions [*Vadas and Fritts*, 2009]. Further details can be found in *Vadas et al.* [2012] and *Vadas and Liu* [2013].

We construct the background atmosphere (for ray tracing) as follows. For $z \leq 25$ km, we utilize the European Centre for Medium-Range Weather Forecasts (ECMWF) ERA-Interim data (available at http://dss.ucar.edu). For $z \geq 35$ km, we utilize the high-resolution TIME-GCM data. We linearly interpolate for $25 \leq z \leq 35$ km. Figures 8a and 8b show the background wind and temperature in the region of the Philippine Islands

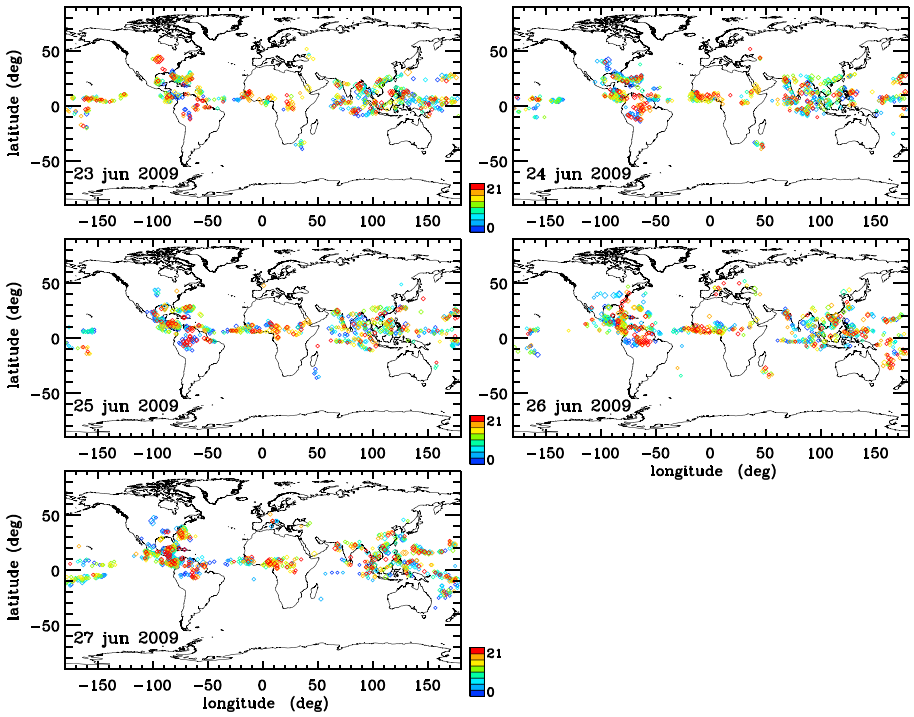

Figure 4. Same as Figure 3 but for 23–27 June 2009.

at 6:00 UT on 18 June 2009 and 2000, respectively. Although the winds are similar, the temperature at $z > 200$ km is much larger in 2000 than in 2009. Figures 8c and 8d show hodographs of the winds at 100°W at northern and southern midlatitudes at 15:00 UT on 18 June 2009 and 2000, respectively. As expected, the winds rotate clockwise (counterclockwise) in the Northern (Southern) Hemisphere (below $z \sim 200$ km) because of the Coriolis force.

In order to calculate the heat/coolings due to GW dissipation, it is necessary to reconstruct the GW field in the thermosphere (as will be shown in section 3.2). (Note that it is possible for this model to calculate the average body forces without reconstruction [e.g., *Vadas and Fritts*, 2006; *Vadas and Liu*, 2009].) Therefore, the GW momentum fluxes, wave vectors, and phases need to be saved on a 4-D "grid" (in x, y, z, and t) in the thermosphere in order to capture the values for each GW as it propagates within this grid. In previous studies, this ray trace model was only employed for regional studies. For example, *Vadas and Liu* [2013] ray traced GWs from convective objects over part of Brazil (45–65°W and 0–20°S). Because this was a regional study, it was possible to use a single grid and still have small enough cell sizes (of 50 km × 50 km × 4 km × 10 min in x, y, z, and t) to obtain adequate resolution. The current study, however, requires a global model. Memory constraints and the fact that our ray trace model employs Cartesian coordinates prevent us from running our ray trace model as a single global grid with small horizontal cell sizes. Additionally, although 50 km horizontal cell sizes are adequate for calculating the body forces (since the forces are determined via calculating the vertical divergence of the GW momentum fluxes, which are automatically saved in the ray trace program) [e.g., *Vadas and Liu*, 2013], horizontal cell sizes of 40 km are needed to calculate the heat/coolings in the thermosphere from GW dissipation. This is because the GW potential temperatures and horizontal/vertical velocities need to be determined fairly accurately via GW reconstruction [*Vadas and Fritts*, 2009], which requires somewhat smaller cell sizes. However, note that the characteristic sizes of the forces and heat/coolings are similar.

One option is to cover Earth with a patchwork of small "Cartesian" grids. This idea was dropped for two reasons. (1) The GWs from plumes within 1500 km of a border between two or more grids would need to be ray traced 2 or more times, thus greatly increasing the computational expense and (2) edge effects would cause the reconstruction of the GW fields to be inaccurate for those plumes within 1500 km of the borders between adjacent grids. Therefore, a different approach was needed.

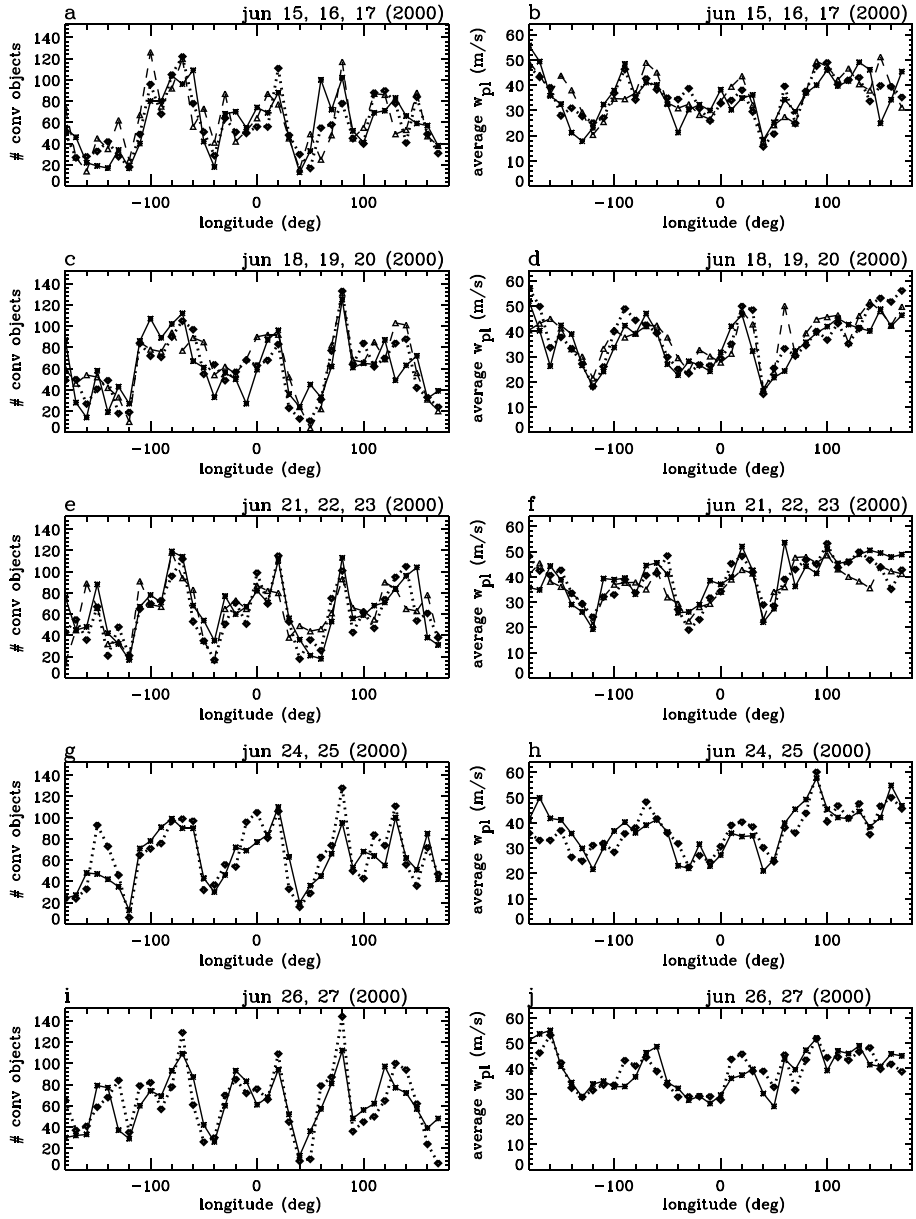

Figure 5. Same as in Figure 2 but for year 2000.

We created a new global fortran-90 ray trace model. For each convective object, we first create a unique Cartesian "patch" or "subgrid" that has cell sizes of 40 km × 40 km × 4 km × 6 min. This patch is centered on the object, has a horizontal domain of 3800 km × 3800 km (in x and y), and spans the altitude range $z = 100$ to 352 km. Thus, there are 95 × 95 grid points in the x and y directions within each patch. Additionally, each patch spans the times $t = 0.2$ to 4.0 h after the plumes within the object overshoot the tropopause. Next, we interpolate all background quantities (e.g., wind and temperature) onto this subgrid. We then ray trace the ~2 million primary GWs excited by the convective object into the mesosphere and thermosphere within this subgrid. (Note that we use 128 × 128 × 256 grid points for each convective object, as described in *Vadas and Fritts* [2009].) If a GW leaves this patch, it is eliminated. After all GWs from a convective object have been ray traced, the GW field within this patch is reconstructed using the GW dissipative polarization relations (see *Vadas and Fritts* [2009]). (Note that ray tracing and reconstruction of the GW field from a single convective object takes ~1–1.5 h on the NASA Pleiades supercomputer.) We then calculate the body forcings and heat/coolings associated with GW dissipation in this patch (see section 3.2). Finally, we interpolate these force/heatings to a lower-resolution "global storage grid." This global grid has cell sizes of

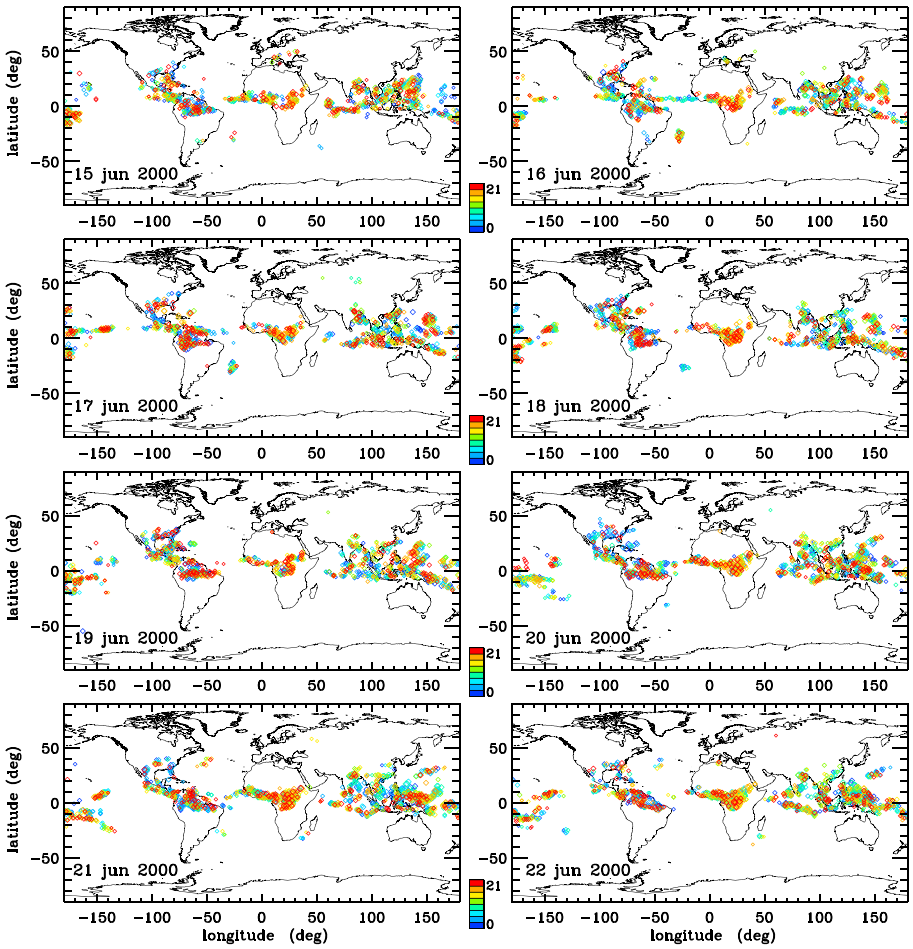

Figure 6. Same as Figure 3 but for 15–22 June 2000.

2.5° × 2.5° × 4 km × 6 min and spans from 180°W to 180°E, 90°S to 90°N, $z = 100$ to 352 km, and $t = 0.2$ to 4.0 h after the plumes within the object overshoot the tropopause. The top boundary of $z = 352$ km was chosen because the amplitudes of the primary GWs are expected to be quite small above $z > 350$ km [*Vadas and Liu*, 2009, 2013; *Vadas*, 2013], thereby leading to negligible force/heat/coolings above $z > 350$ km. This interpolation takes into account periodic boundary conditions in longitude and goes over the poles (if the convective object is near a pole). This solution is then added linearly to the total global solution. Finally, the unique patch (subgrid) created for this object is eliminated. We perform this procedure for all convective objects at a specific time (e.g., 15 UT on 16 June 2000) and save the results in a file. We then perform this procedure for all convective objects within the 13 day study period.

As mentioned earlier, full-disk IR satellite images were only available every 3 h. Therefore, we only ray traced primary GWs from convective objects every 3 h. However, new convective plumes are typically created every ~20–30 min [*Vadas et al.*, 2012; *Vadas and Liu*, 2013]. Therefore, if we do not interpolate our solutions to 20–30 min "in-between" times, the calculated force/heat/coolings will have an unphysical 3 h periodicity and will have amplitudes that are too small. Therefore, we assume that similar convective objects overshot the tropopause every 30 min, and so linearly interpolate our ray trace solutions to 30 min in-between times. For example, to obtain the solution at time $= t + \Delta t = t + 30$ min, i.e., $g_{\Delta t}(t + \Delta t)$, for the (unray traced) convective objects that likely overshot the tropopause at 00:30 UT on 15 June, we utilize the ray traced "A" solution created by the convective objects that overshot the tropopause at 00:00 UT on 15 June, (i.e., $g_A(t)$) and the ray traced "B" solution created by the convective objects that overshot the tropopause at 03:00 UT on 15 June, (i.e., $g_B(t + T)$), where $T = 3$ hrs and $\Delta t = 30$ min. Here "g" can be any GW quantity, such as temperature perturbation, vertical velocity, etc. Then the interpolated solution $g_{\Delta t}$ at time $t + \Delta t$ created

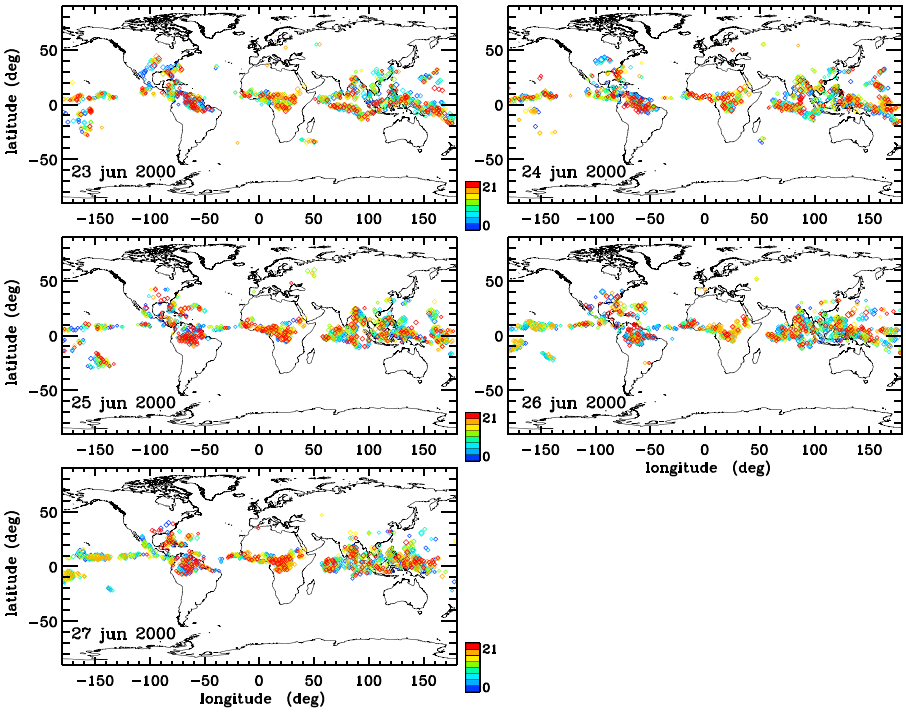

Figure 7. Same as Figure 6 but for 23–27 June 2000.

by the convective objects which likely overshot the tropopause at Δt (i.e., at 00:30 UT) (but which were not quantified due to lack of satellite images at 00:30 UT) is

$$g_{\Delta t}(t+\Delta t) = (1-\Delta t/T)\ g_A(t) + (\Delta t/T)\ g_B(t+T). \tag{1}$$

We similarly obtain the solution at time $= t + \Delta t$ for the objects which likely overshot the tropopause at 01:00, 01:30, 02:00, and 02:30 UT via setting $\Delta t = 1$, 1.5, 2, and 2.5 h, respectively, in equation (1). The same procedure is performed every 30 min throughout each day. All solutions are then added together to create the total solution. These solutions include the average nondimensional amplitude squared in each 4-D cell. We then reray trace all primary GWs again in order to include the effects of GW saturation (or parameterized wave breaking) using Lindzen's scheme [*Lindzen*, 1981; *Vadas and Liu*, 2013]. This has the effect of reducing the amplitudes of the primary GWs that break in the thermosphere [*Lund and Fritts*, 2012].

Finally, a note of caution. All secondary GW, tidal, and "mean" horizontal wind effects (described below) are approximately proportional to the amplitudes of the body force/heatings. Thus, if these amplitudes are overestimated by a factor of 2, then the resultant effects will also be overestimated by a factor of 2. Although we are utilizing the high-resolution TIME-GCM, it may not simulate large-enough winds in the upper mesosphere [*Larsen and Fesen*, 2009]. Smaller mesosphere/lower thermosphere winds likely cause less primary GW wind filtering, which may result in larger thermospheric body force/heating amplitudes.

3.2. Body Force/Heat/Coolings Created From the Dissipation of Primary GWs

The effect of GW dissipation on the mean wind can be described by the horizontal components of the Reynolds stress tensor [*Bretherton*, 1969]. Heat/cooling also accompanies GW dissipation [*Walterscheid*, 1981; *Liu*, 2000; *Becker*, 2004; *Yiğit and Medvedev*, 2009]. The spatially and temporally varying zonal and meridional components of the body force and heat/cooling (per unit mass) are [*Becker*, 2004; *Vadas*, 2013]:

$$F_{x,\mathrm{tot}} = -\frac{1}{\overline{\rho}}\frac{\partial(\overline{\rho}\,\overline{u'w'})}{\partial z}, \quad F_{y,\mathrm{tot}} = -\frac{1}{\overline{\rho}}\frac{\partial(\overline{\rho}\,\overline{v'w'})}{\partial z}, \tag{2}$$

$$J_{\mathrm{tot}} = -\frac{1}{\overline{\rho}}\frac{\partial}{\partial z}\left(\frac{\overline{\rho}\,\overline{T}}{\overline{\theta}}F_\theta\right) - \frac{g}{C_p}\frac{F_\theta}{\overline{\theta}} + \frac{\nu}{C_p}\overline{\left(\frac{\partial}{\partial z}\mathbf{v}'\right)^2}, \tag{3}$$

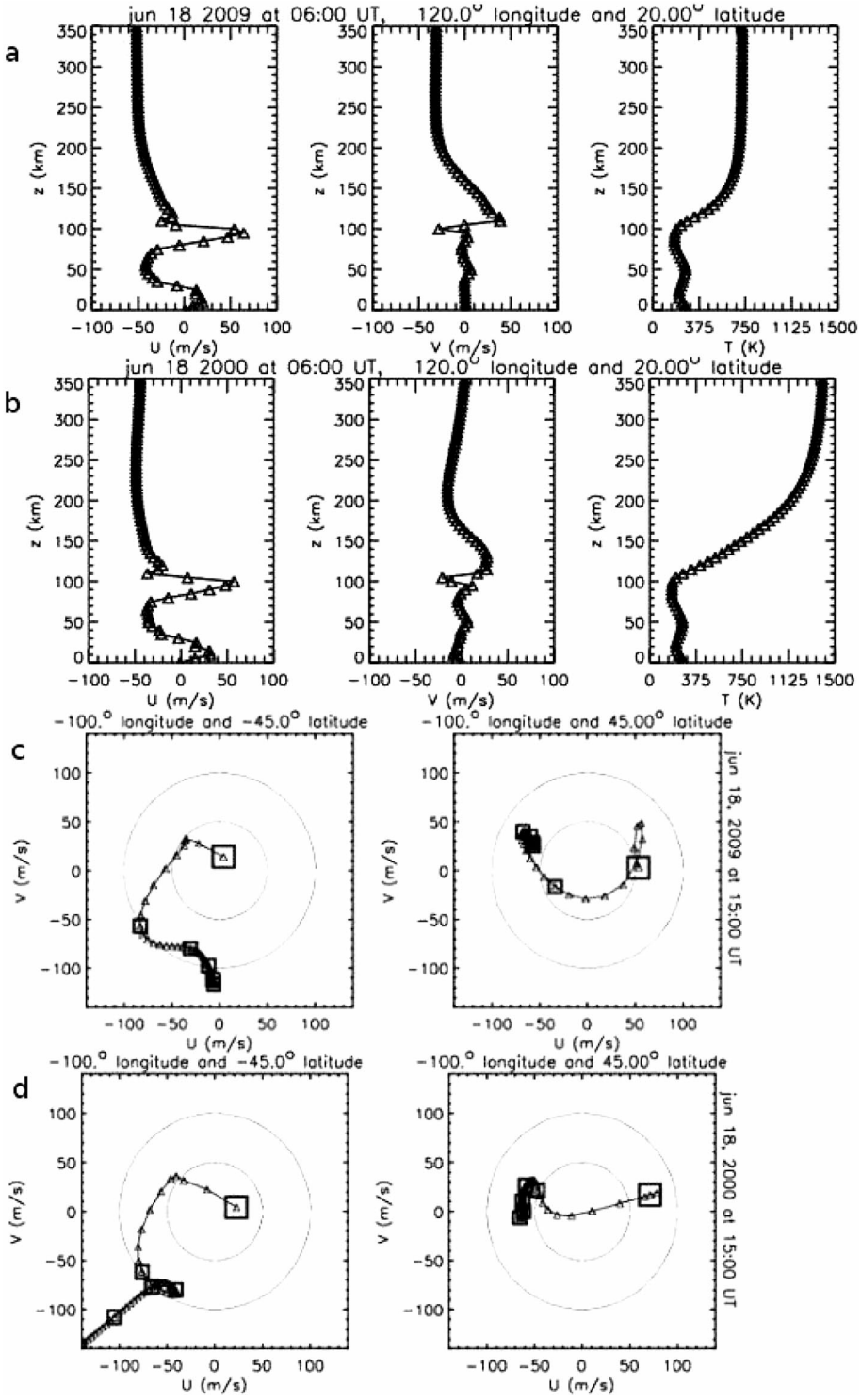

Figure 8. (a) Background zonal wind, meridional wind, and temperature at 120° E and 20° N on 18 June 2009 at 06:00 UT. (b) Same as Figure 8a but in year 2000. (c) Hodograph of the background horizontal wind from $z = 100$ to 350 km on 18 June 2009 at 15:00 UT at 100°W and 45°S (left) and 100°W and 45°N (right). The large square denotes the wind at $z = 100$ km, the triangles are every 5 km vertically, and the medium squares are every 50 km vertically. (d) Same as Figure 8c but in year 2000.

Table 2. TIME-GCM Runs

GW Effects Included From Ray Tracing	Run Name
none	nogwf
$F_{x,\mathrm{tot}}, F_{y,\mathrm{tot}}$ only	gwfuv
J_{tot} only	gwft
$F_{x,\mathrm{tot}}, F_{y,\mathrm{tot}}$, and J_{tot}	gwfuvt

respectively, where the vertical flux of potential temperature is

$$F_\theta = \overline{\theta' w'}, \tag{4}$$

overlines denote averages over several wavelengths, $\mathbf{v}' = (u', v', w')$ is the velocity vector perturbation, $\theta = T(p_s/p)^{(\gamma-1)/\gamma}$ is the potential temperature, $T = \overline{T} + T'$ is the temperature, p_s is the standard pressure, $p = \overline{p} + p' = \mathrm{r}\rho T$ is the pressure, $\rho = \overline{\rho} + \rho'$ is the neutral density, g is the gravitational acceleration, $C_p = \gamma R/(\gamma - 1)$ is the mean specific heat at constant pressure, and ν is the kinematic viscosity. Here $\overline{\rho}$, $\overline{p}$, $\overline{\theta}$, and $\overline{T}$ are the background density, pressure, potential temperature, and temperature, respectively. Additionally, $F_{x,\mathrm{tot}}$ and $F_{y,\mathrm{tot}}$ are the zonal and meridional components of the body force induced by the dissipating GWs (in m/s^2), respectively, and J_{tot} is the heat/cooling induced by the dissipating GWs (in K/s). If $J_{\mathrm{tot}} > 0$ ($J_{\mathrm{tot}} < 0$), the fluid is being heated (cooled). If the GWs are not dissipating or saturating, (1) ($\overline{\rho}\,\overline{u'w'}$) and ($\overline{\rho}\,\overline{v'w'}$) are constant with altitude, so that $F_{x,\mathrm{tot}} = F_{y,\mathrm{tot}} = 0$, and (2) θ' and w' are in quadrature according to linear Boussinesq theory (if the GWs are small-scale) [e.g., *Fritts and Alexander*, 2003], so that $F_\theta = 0$ and $J_{tot} = 0$. The first term on the right-hand side of equation (3) is the "heat flux convergence", which creates the heat/cooling dipoles at $z \sim$ 150–200 km described by *Vadas* [2013]. The second term is the buoyancy production of GW kinetic energy, which is generally unimportant [*Vadas*, 2013]. The third term is the dissipation of GW kinetic energy due to molecular viscosity, which can lead to substantial heating at $z \sim$ 200–300 km [*Vadas*, 2013].

4. Large-Scale Changes to the Thermosphere and Ionosphere From the Dissipation of GWs From Deep Convection

Using the new global ray trace model described in section 3, we calculated the thermospheric body forces and heat/coolings which resulted from the dissipation of primary convectively generated GWs during the 13 day study periods. We now determine the large-scale changes that occur in the thermosphere and ionosphere as a result of these force/heatings.

4.1. Input of Force/Heatings Into the Global TIME-GCM

In order to study the large-scale changes which result from the force/heatings, we utilize the TIME-GCM. The TIME-GCM simulates the wind circulation, temperature, and compositional structures of the upper atmosphere ($z \sim$30–500 km) and the ionosphere and includes the dynamical, chemical, and electrodynamical processes in that atmospheric region [*Roble and Ridley*, 1994]. Tidal perturbations are specified at the lower boundary of TIME-GCM with monthly tidal climatology from the global scale wave model (GSWM-02) [*Hagan and Forbes*, 2002, 2003]. Migrating and nonmigrating tides propagating in both westward and eastward directions, with diurnal and semidiurnal periods and wave numbers 0–6, are provided by GSWM-02. The TIME-GCM mean state at the lower boundary is specified by the daily averaged geopotential height, neutral temperature, and horizontal winds from the ECMWF data. We run the TIME-GCM at high resolution (four grids/scale height and 2.5° × 2.5°). The grid spacing is ~250 km near the equator. Although GWs with horizontal wavelengths $\geq$ 500 km could be resolved in theory, this model can only resolve secondary GWs with horizontal wavelengths > 2000 km because of added numerical viscosity [*Vadas and Liu*, 2009].

Because the TIME-GCM includes a GW parameterization scheme up to $z = 120$ km (which we retain in all runs), we smoothly zero out our calculated force/heatings for $z < 120$ km in order to avoid double counting the GW effects [*Vadas and Liu*, 2013]. The force/heatings are then interpolated in space and time into the high-resolution TIME-GCM for all runs except nogwf (see below). We perform four TIME-GCM runs here. The first is with no GW force/heating (dubbed "nogwf"). The second is with GW momentum flux divergence (i.e., body forcing) only ($F_{x,\mathrm{tot}}, F_{y,\mathrm{tot}}$ nonzero, $J_{\mathrm{tot}} = 0$, dubbed "gwfuv"). The third is with GW heat/cooling only (J_{tot} nonzero, $F_{x,\mathrm{tot}} = F_{y,\mathrm{tot}} = 0$, dubbed "gwft"). The forth is with all GW effects included ($F_{x,\mathrm{tot}}, F_{y,\mathrm{tot}}$, and J_{tot} nonzero, dubbed "gwfuvt"). Table 2 summarizes these runs. In the next few sections, we show the large-scale responses to these GW force/heatings. The plotted quantities show the "perturbed" TIME-GCM solutions (gwfuv, gwft, or gwfuvt) minus the "unperturbed" TIME-GCM solutions (nogwf).

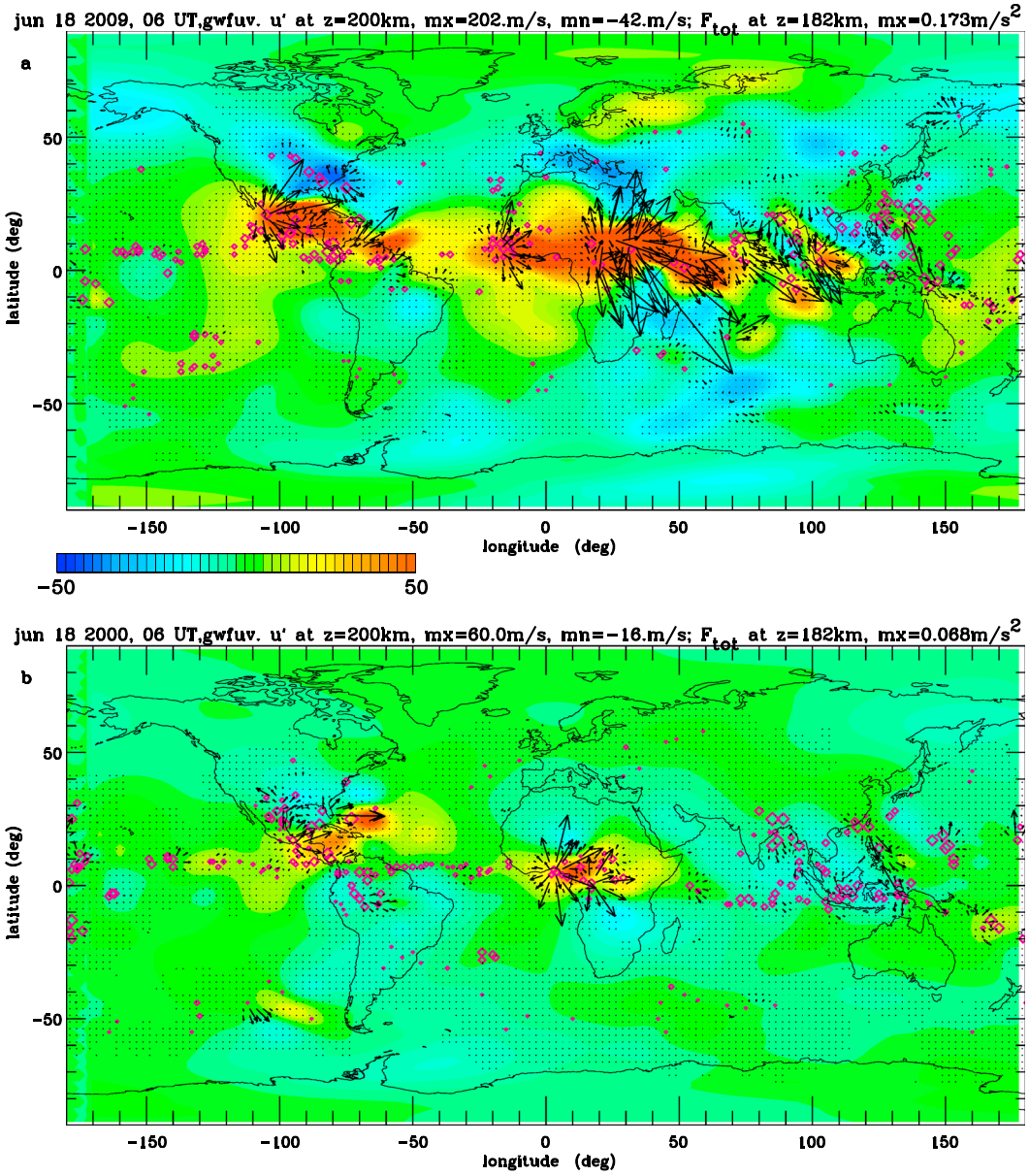

Figure 9. (a) The zonal wind perturbation from the TIME-GCM, u' (gwfuv-nogwf), on 18 June 2009 at 06:00 UT and $z = 200$ km. u' is shown as blue (−50 m/s) to red (+50 m/s) in intervals of 2.5 m/s. The maximum (minimum) value of u' is 202 m/s (−42 m/s). The horizontal body forces ($F_{x,\mathrm{tot}}, F_{y,\mathrm{tot}}$) are shown at $z = 182$ km as vectors, with a maximum of 0.173 m/s^2. Diamonds show the convective objects at 6 UT, with sizes proportional to w_{pl}. (b) Same as in Figure 9a but for year 2000. The maximum (minimum) value of u' is 60 m/s (−16 m/s). The body force maximum is 0.068 m/s^2.

4.2. Large-Scale Changes to the Thermosphere

We now examine the large-scale changes that occur in the thermosphere from the convectively generated force/heatings.

4.2.1. Changes to the Thermosphere From Horizontal Body Forces Only

We first examine the changes to the thermosphere which result from the horizontal body forces only. Figure 9a shows a representative case. Here we show the zonal wind perturbation, u' (gwfuv-nogwf), on 18 June 2009 at 06:00 UT and $z = 200$ km. This altitude is chosen because it is near the altitude where the body forces maximize and thus create the largest horizontal wind perturbations. The largest zonal wind perturbations are eastward (positive) and occur near the equator (especially over Africa, India, and Central America), near the occurrence of strong deep convection (pink diamonds). The maximum (pinpoint) value

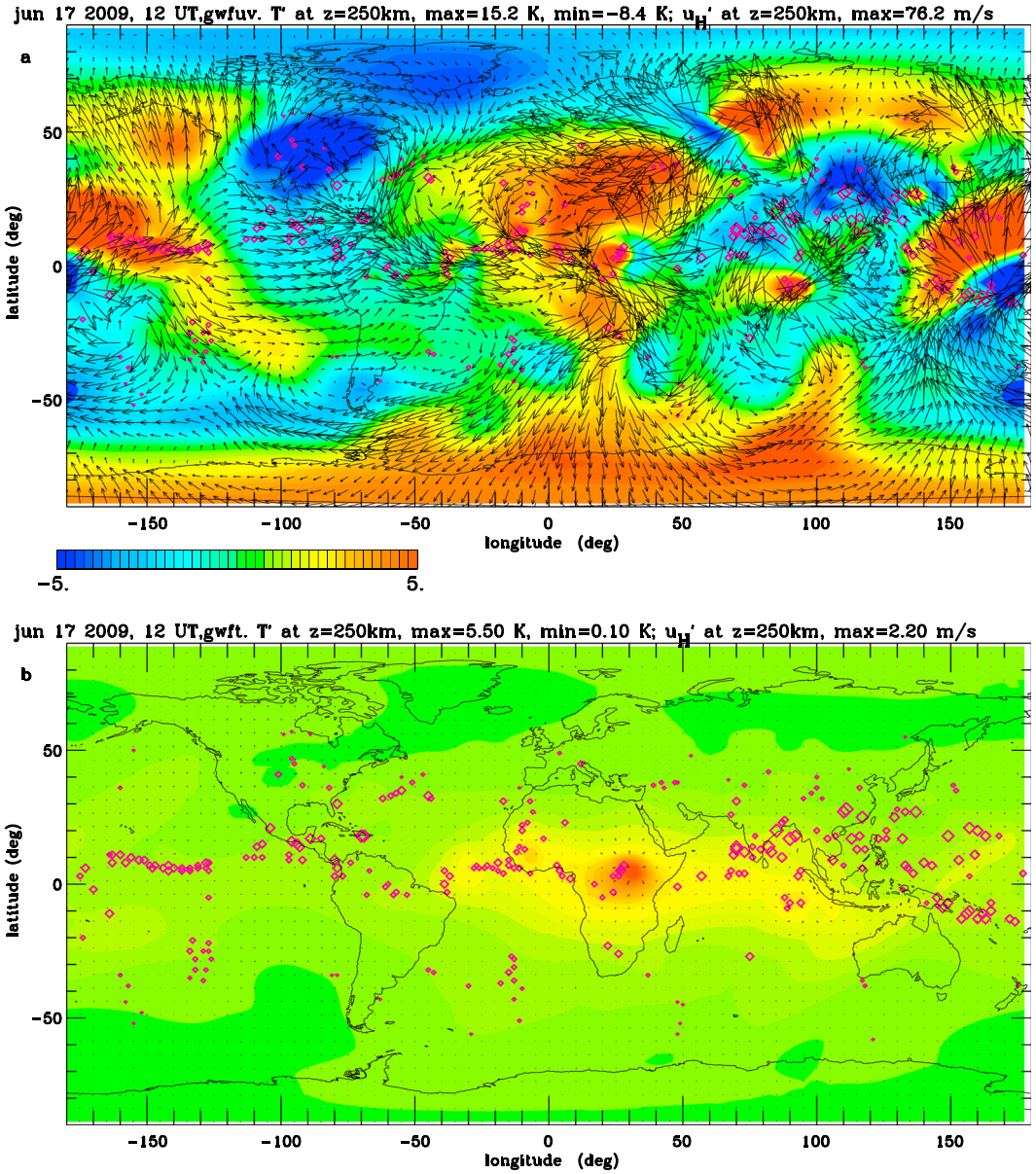

Figure 10. (a) The neutral temperature perturbations from the TIME-GCM, T' (gwfuv-nogwf), on 17 June 2009 at 12:00 UT and $z = 250$ km. T' is shown as blue (−5 K) to red (+5 K) in intervals of 0.25 K. The maximum (minimum) value of T' is 15.2 K (−8.4 K). The horizontal wind perturbation, u'_H (gwfuv-nogwf), is shown at $z = 250$ km as vectors, with a maximum of 76.2 m/s. Diamonds show the convective objects as in Figure 9. (b) Same as in Figure 10a but for gwft-nogwf. The maximum (minimum) value of T' is 5.5 K (0.1 K). The maximum value of u'_H is 2.2 m/s.

is $u' = 200$m/s, which tends to be much larger than the background zonal wind from the tides at this altitude and latitude. (Note that such a high value might not be easily observed because of temporal and spatial smoothing that are typically performed on wind data.) Typical zonal wind perturbations are seen to be $u' \sim 30$–60m/s in Figure 9a. The largest westward wind perturbations occur at northern midlatitudes where deep convection is sparse. Its maximum amplitude is $u' \sim -42$ m/s. We can understand the origin of these eastward and westward winds by examining the horizontal body forces, which are shown as vectors at $z = 182$ km in Figure 9a. These forces are spatially localized and are strongest near the equator, where they are mostly eastward because of preferential wind filtering from westward equatorial background winds at $z \sim 150$ km. These eastward forces drive strong eastward wind perturbations. However, because the horizontal body forces have finite zonal extents (typically 10–40°), the fluid will diverge near the eastern "edge"

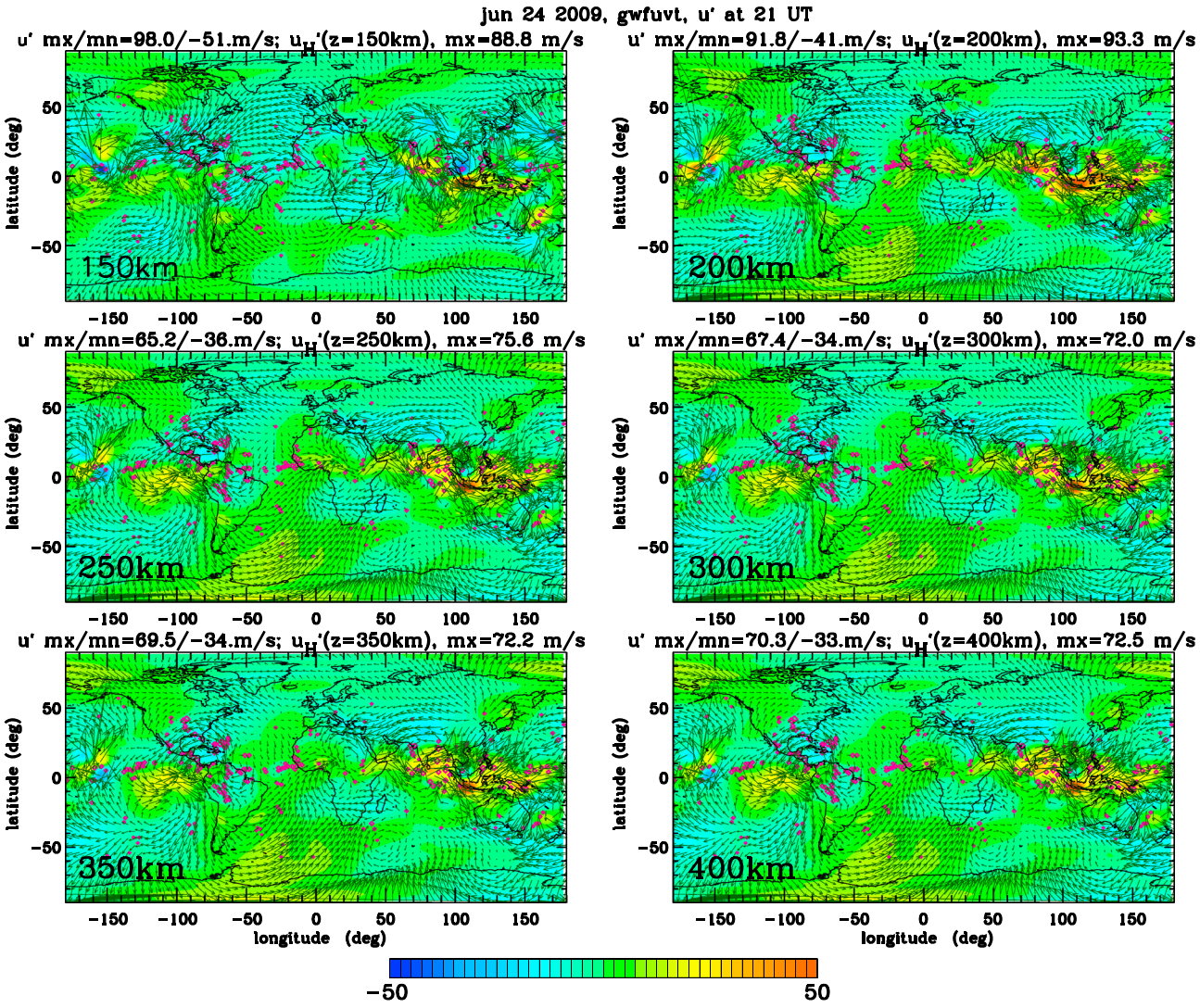

Figure 11. (from left to right, upper to lower rows) The zonal wind perturbation from the TIME-GCM, u' (gwfuvt-nogwf), on 24 June 2009 at 21 UT from z = 150 to 400 km every 50 km as labeled. u' is shown as blue (−50 m/s) to red (+50 m/s) in intervals of 2.5 m/s. We overplot the horizontal wind perturbation u'_H (gwfuvt-nogwf) as vectors. The maximum/minimum values of u' and the maximum values of u'_H are listed at the top of each panel. Pink diamonds show the convective objects.

of an eastward body force, with approximately half turning northward and the other half turning southward. The fluid then moves westward at northern and southern midlatitudes, finally turning south/northward at the western edge of the force to rejoin the eastward wind near the equator. These motions describe two counter-rotating circulation cells that are centered on the force [*Vadas and Liu*, 2009, 2013].

We note that the tendency for an eastward wind perturbation at equatorial latitudes and a westward wind perturbation at midlatitudes is a typical model result *at this altitude* throughout the 13-day period. This is because the equatorial background winds are primarily westward at $z \sim$ 150 km, causing eastward primary GWs to dissipate at $z \sim$ 180–190 km (due to wind filtering), thereby leading primarily to equatorial eastward forces. These eastward forces create eastward wind perturbations where the forces are located. The midlatitude westward wind perturbations are then part of the return fluid flow (which creates the counter-rotating circulation cells). This return flow is caused by mass conservation of the induced eastward flow, not GW wind filtering at midlatitudes, and occurs because these forces have finite longitudinal extents. The finite longitudinal extents occur because deep convection has strong longitudinal variability (e.g., Figure 2). (Note: if the forces had been zonally and latitudinally symmetric, there would not have been midlatitude return flows).

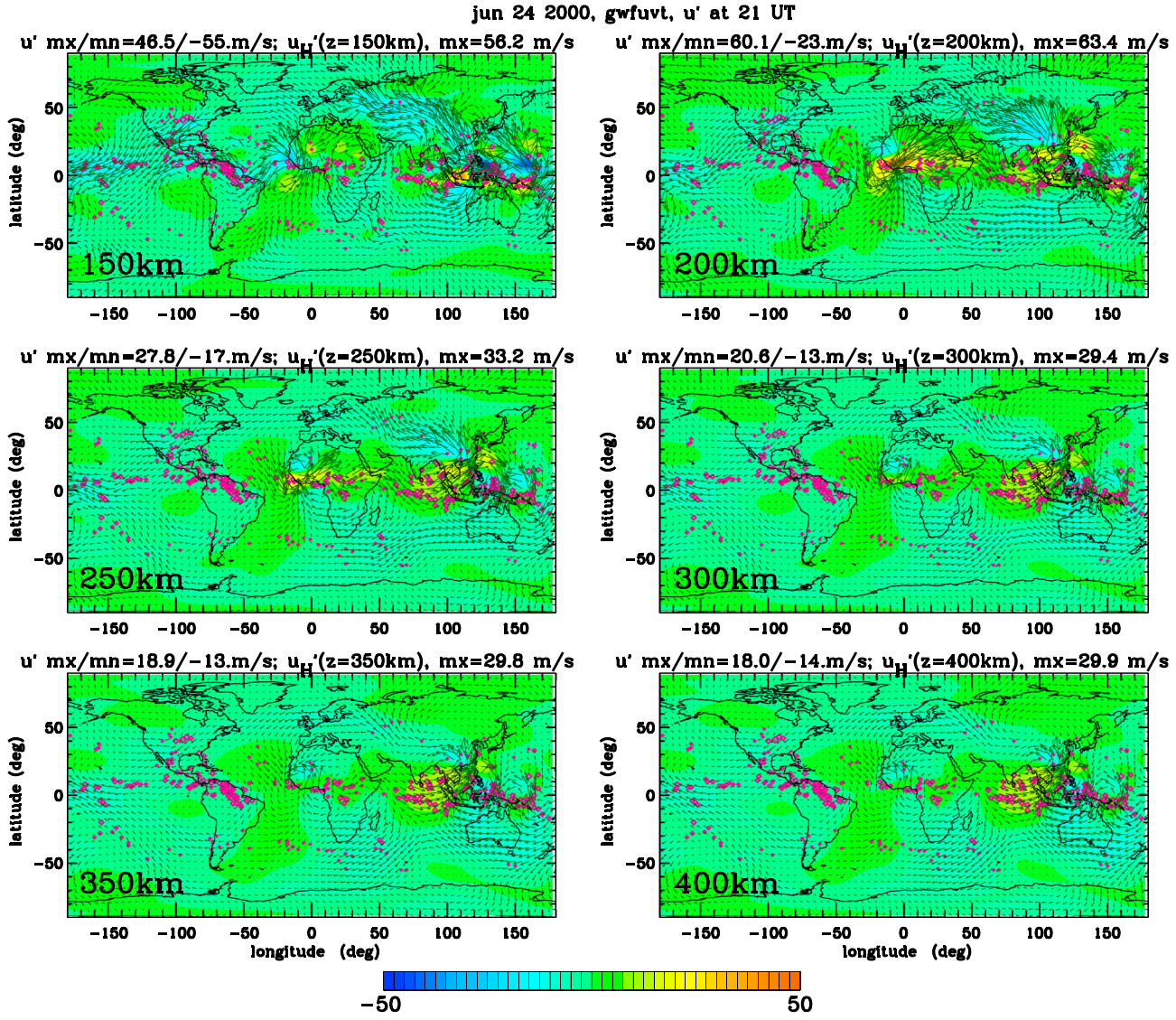

Figure 12. Same as Figure 11 but for 2000.

Figure 9b shows the same day/time/altitude but in 2000. As in 2009, there are eastward wind perturbations near the equator (over Africa and Central America) and westward wind perturbations at midlatitudes. However, the maximum values of u' are smaller here, $u' = 60$m/s. This occurs because the maximum horizontal force in Figure 9a is 0.17 m/s^2, whereas it is 2.5 times smaller in Figure 9b (i.e., year 2009): 0.068 m/s^2. It is a typical result that the zonal wind perturbations are much larger in 2009 (at all days and times) than in 2000, and it occurs because the body force amplitudes are smaller during solar maximum than solar minimum. This occurs because the kinematic viscosity increases less rapidly with altitude during solar maximum (because the temperature increases more rapidly with altitude). During solar maximum then, the primary convective GWs dissipate over a larger vertical depth because of this more gradual increase in the kinematic viscosity. However, during solar minimum, the kinematic viscosity increases much more rapidly with altitude, thereby acting like a "wall" for GWs attempting to propagate to higher altitudes in the thermosphere. This causes the primary convective GWs to dissipate over a much smaller vertical depth during solar minimum. This leads to larger body force amplitudes during solar minimum than during solar maximum, thereby confirming and generalizing an earlier idealized study involving a single convective plume [*Vadas and Fritts*, 2006]. Note that the altitudes where the forces are maximum are similar during solar minimum and maximum ($z \sim$180–200 km), thereby confirming and generalizing this same earlier idealized study [*Vadas and Fritts*, 2006].

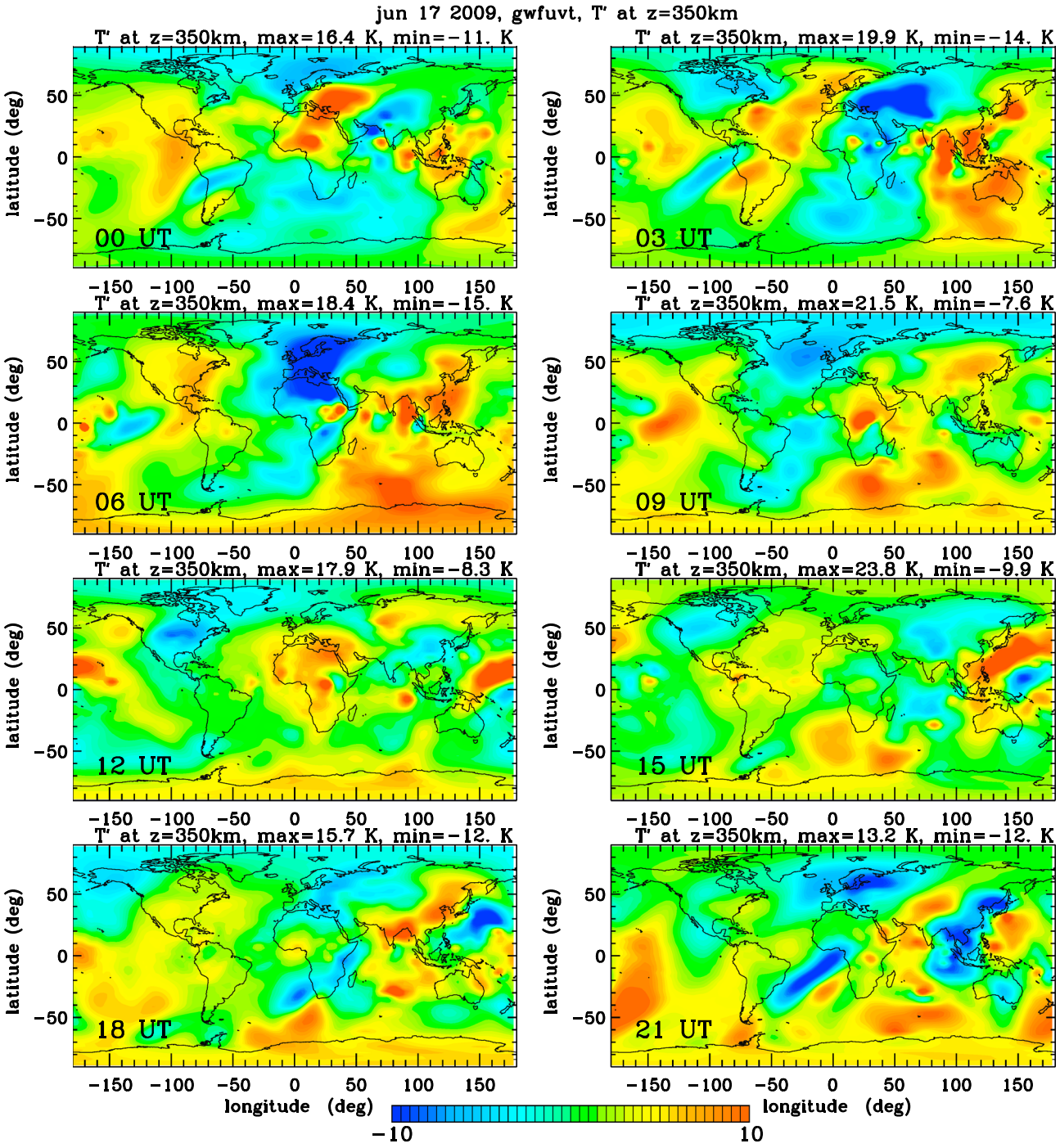

Figure 13. The neutral temperature perturbation from the TIME-GCM, T' (gwfuvt-nogwf), worldwide on 17 June 2009 at $z = 350$ km every 3 h, as labeled. T' is shown as blue (−10 K) to red (+10 K) in intervals of 0.5 K. The maximum (minimum) value of T' is listed at the top of each panel.

4.2.2. Changes to the Thermosphere From Heat/Cooling Only

Up to this point, convective plume studies have only included the effects of body forces arising from GW dissipation on the dynamics of the thermosphere [*Vadas and Liu*, 2009, 2013]. However, *Yiğit and Medvedev* [2009] argued that the heat/cooling arising from GW dissipation in the thermosphere could not be neglected and might lead to large temperature changes. *Vadas* [2013] estimated heat/cooling rates of 0.06 to 0.15 K/s for solar maximum and minimum, respectively, from a single energetic plume. Therefore, we now examine how the heat/coolings from convection worldwide affect the thermosphere.

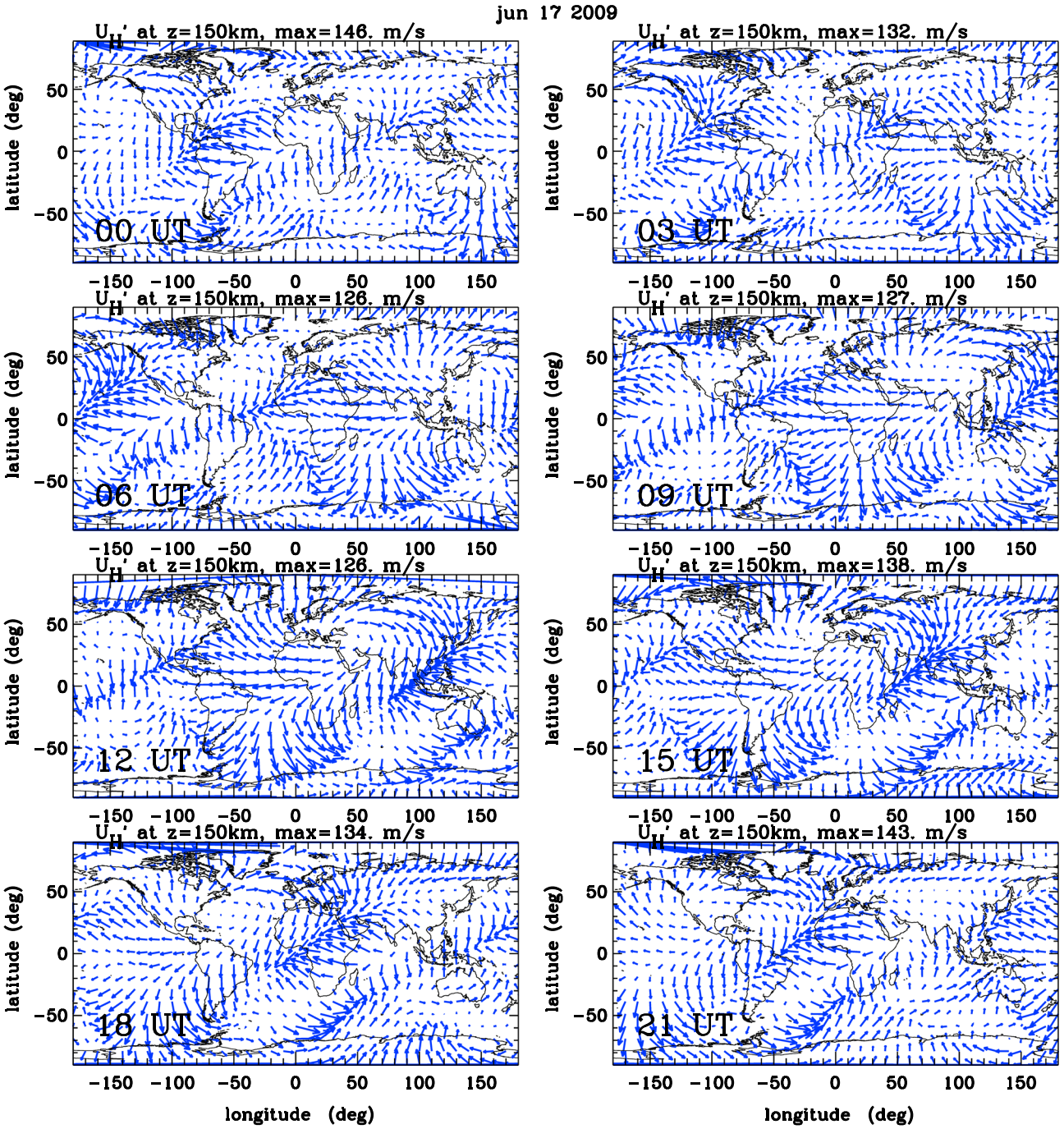

Figure 14. The neutral background wind from the nogwf TIME-GCM (blue vectors), worldwide on 17 June 2009 at z = 150 km every 3 h, as labeled. The maximum (minimum) value of T' is listed at the top of each panel.

We first examine the temperature changes that occur from the body forces only. Figure 10a shows the neutral temperature perturbations, T' (gwfuv-nogwf), on 17 June 2009 at 12:00 UT and at z = 250 km. The maximum value of T' is 15.2 K. The induced horizontal wind perturbation, u'_H (gwfuv-nogwf), is also shown at z = 250 km. u'_H is mainly eastward near the equator, although there is a small region at 100°E where it is westward. Many rotating cells are seen. The maximum amplitude of the wind perturbation is u'_H = 76.2 m/s. This altitude, z = 250 km, is chosen in order to compare with Fabry-Perot wind and temperature measurements, although those observations are integrated over the thickness of the 630 nm layer (i.e., $z \sim$ 220–280 km) [e.g., *Makela et al.*, 2011; *Nicolls et al.*, 2012; *Chapagain et al.*, 2012]. Note that the

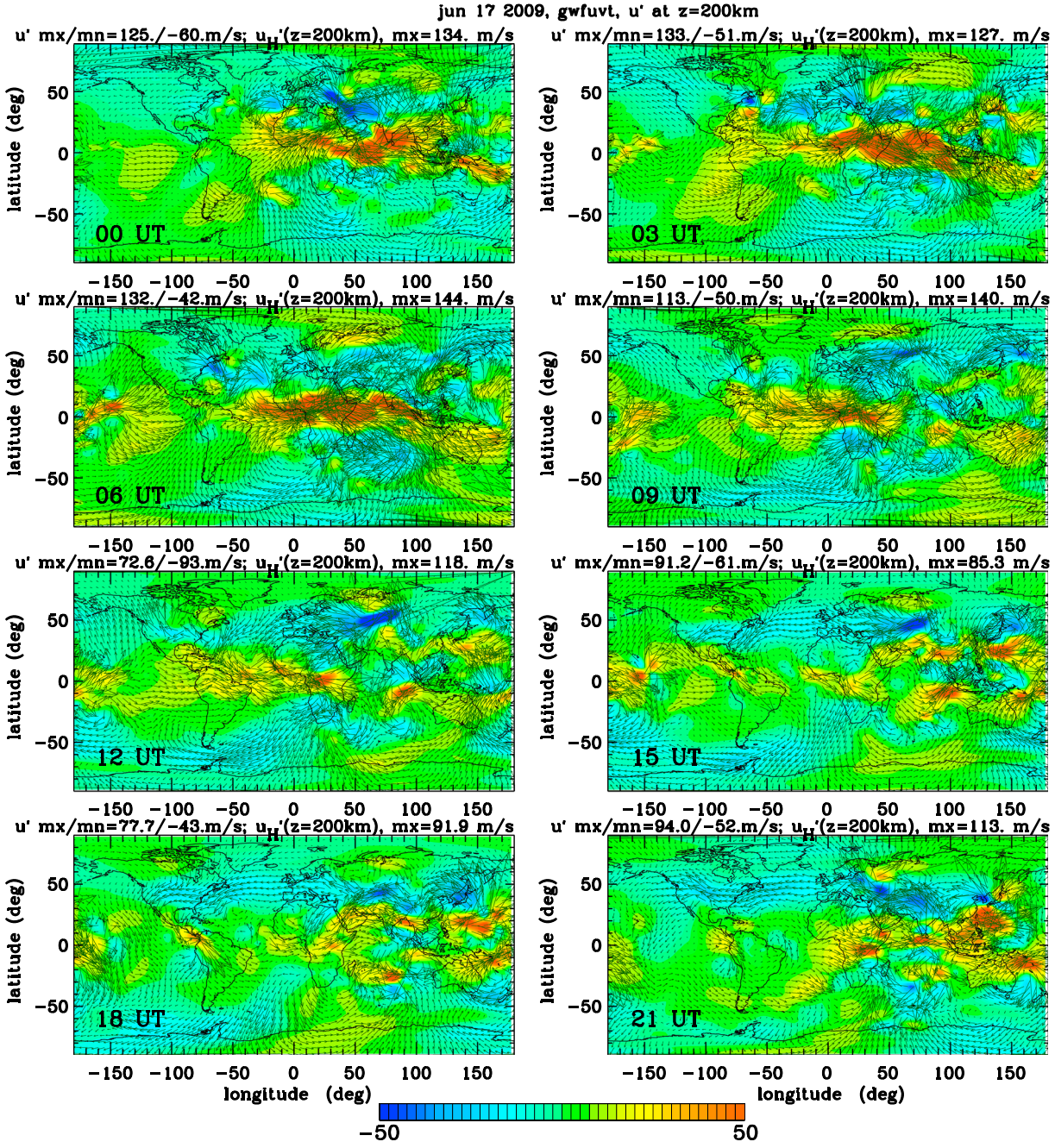

Figure 15. The zonal wind perturbation from the TIME-GCM, u' (gwfuvt-nogwf), on 17 June 2009 at $z = 200$ km every 3 h, as labeled. u' is shown as blue (−50 m/s) to red (+50 m/s) in intervals of 2.5 m/s. We overplot the horizontal wind perturbation u'_H (gwfuvt-nogwf) as vectors. The maximum/minimum values of u' and the maximum values of u'_H are listed at the top of each panel.

maximum wind perturbation amplitudes are generally smaller at $z = 250$ km than at $z = 200$ km because the perturbations at $z \sim 250$ km ($z \sim 200$ km) are primarily associated with the secondary GWs (wind perturbations created by the body forces). In a moment, we will show the horizontal wind as function of altitude on a different time and day (see Figure 11).

Next, we examine the temperature changes that occur from the heat/coolings only. Figure 10b shows T' (gwft-nogwf) for the same day, time, and altitude. The resulting temperature perturbations are ~65% smaller, with a maximum of 5.5 K. Additionally, the maximum value of the horizontal velocity perturbations is quite small: $u'_H = 2.2$ m/s.

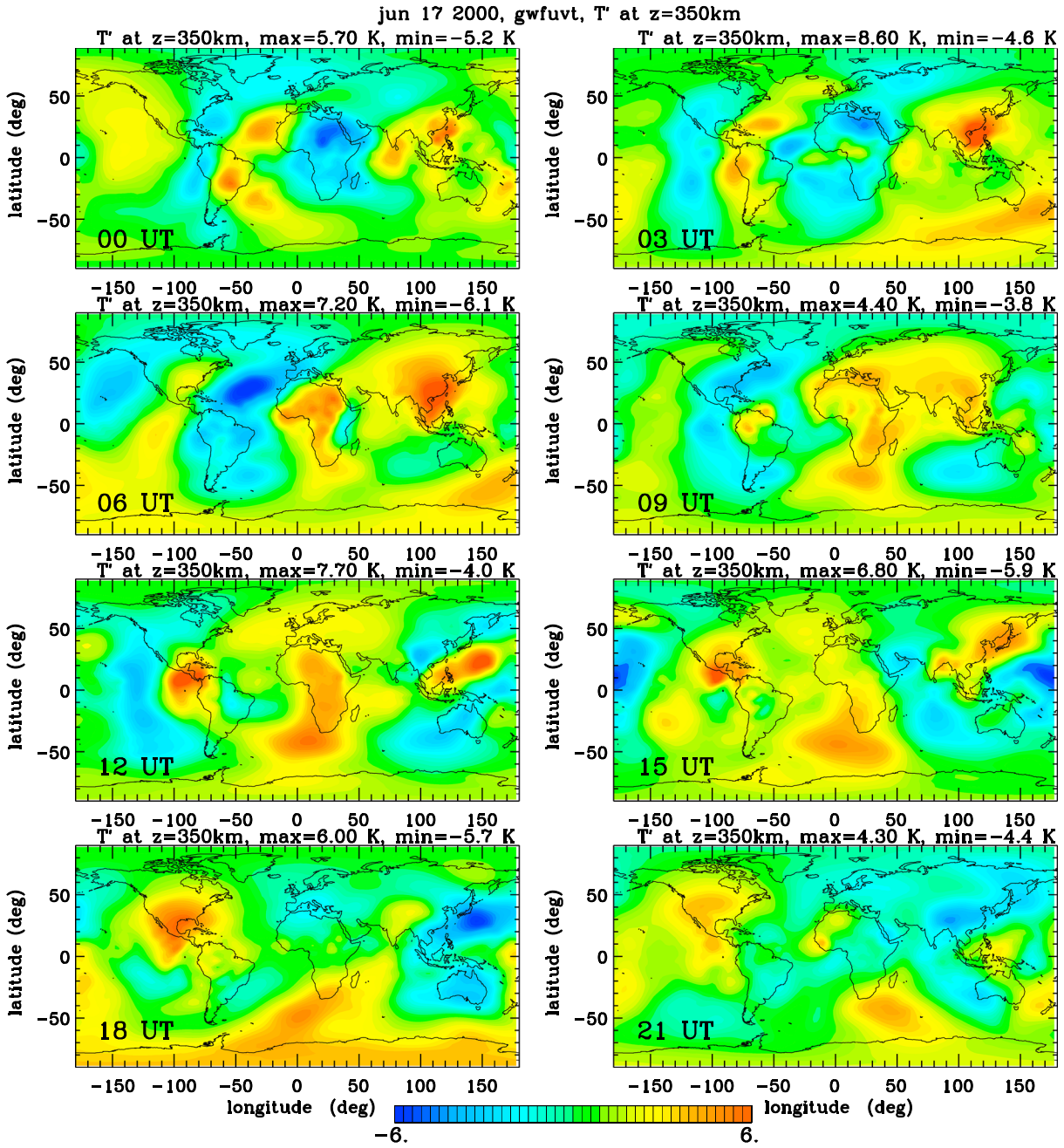

Figure 16. Same as Figure 13 but for 2000. T' is shown as blue (−6 m/s) to red (+6 m/s) in intervals of 0.3 K.

We examined the results every 3 h over the 13 day study period in 2009. For the gwfuv runs, the maximum temperature perturbations are max(T') ~10–40 K and the average maximum value is $\overline{\max(T')}$ ~18 K at z = 150 km, while at z = 200 and 250 km, max(T') ~10-30 K and $\overline{\max(T')}$ ~14 K. For the gwft runs $\overline{\max(T')}$ ~1–4 K and $\overline{\max(T')}$ ~2 K at z = 150 km, while at z = 200 and 250 km, max(T') ~2–7 K and $\overline{\max(T')}$ ~3 K. For the (total) gwfuvt runs in 2009, the results are nearly the same as the gwfuv results, with max(T') ~10–40 K and $\overline{\max(T')}$ ~15–19 K at z = 150–250 km.

Therefore in general, (1) the maximum temperature perturbations created by the heat/coolings are only ~10–25% that created by the body forces and (2) the horizontal wind perturbations created by the heat/coolings are quite small.

For the rest of this paper, we only show the results for gwfuvt-nogwf.

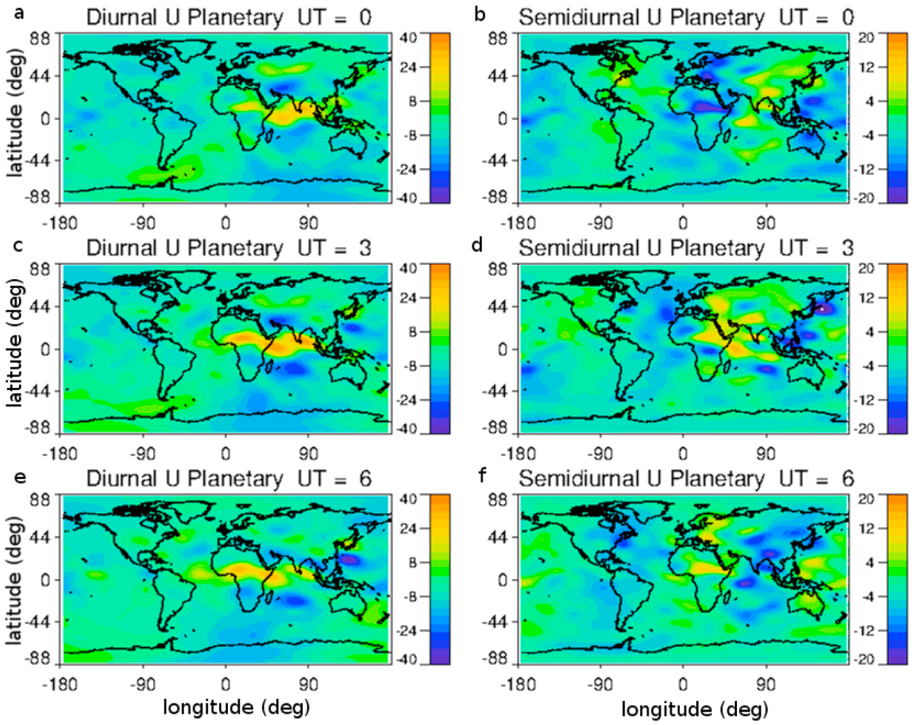

Figure 17. (a, c, and e) Diurnal and (b, d, and f) semidiurnal zonal wind perturbation u' synthesized from $s = 0$ and eastward and westward traveling zonal wave numbers 1–10. Here u' is from the TIME-GCM, u' (gwfuvt-nogwf), mapped at 00 UT (Figures 17a and 17b), 03 UT (Figures 17c and 17d) and 06 UT (Figures 17e and 17f) on 17 June 2009 at $z = 250$ km.

4.2.3. Variations of the Horizontal Wind Perturbations With Altitude

Figure 11 shows the induced zonal (u') and horizontal (u'_H) wind perturbations at $z = 150$ to 400 km in 50 km intervals on 24 June 2009 at 21 UT (gwfuvt-nogwf). Regions of large horizontal wind perturbations are apparent and are highly correlated with regions of deep convective overshoot at the tropopause (pink diamonds), as expected. In each significant region of deep convection (i.e., where a few or more convective objects occur), circular horizontal motions occur. These circular motions are both clockwise and counterclockwise, with spatial extents for the circulation cell pairs of 1000–5000 km. Similar cells were seen previously in a model study involving a single thermospheric force created by a single plume [*Vadas and Liu*, 2009]. Additionally, we see that regions of large $|u'_H|$ are highly correlated with significant regions of deep convective activity *at all altitudes*, as expected. For example, the counterclockwise wind perturbations seen at 80°W and 20°N over Central America at $z = 200$ km persist up to $z = 400$ km and the westward wind perturbations seen at 60–80°E and 30–50°N at $z = 200$ km persist up to $z = 400$ km. Additionally, the magnitudes of the induced wind perturbations at $z = 400$ km are only slightly smaller than the magnitudes at $z \sim 200$ km; the maximum (pinpoint) values at $z = 200$ and 400 km are $u'_H = 94$ and 73 m/s, respectively. Typical values of u'_H are one half of the maximum value, or $u'_H \sim 35$–45 m/s. Note that these values are not averaged spatially or temporally and are similar to the amplitude of the background wind (see Figure 8). Thus, the horizontal wind perturbations created by the dissipation of convectively generated GWs are predicted to be quite significant at $z = 200$ to 400 km. Note that these horizontal wind perturbations are a combination of mean winds and secondary GWs [*Vadas and Liu*, 2009, 2013].

In *Vadas and Liu* [2009, 2013], we showed that the body forces created by the dissipation of convectively generated GWs are maximum at $z \sim 180$–190 km and are negligible for $z \geq 300$ km. Additionally, *Vadas* [2013] showed that the heat/coolings created by the dissipation of convectively generated GWs are only important for $z \leq 300$ km. Thus, Figure 11 demonstrates that the wind perturbations created by GW dissipation is quite significant well above the altitude where the winds are directly accelerated by the body forces and/or are directly created by the heat/coolings. These wind perturbations are a combination of mean winds and secondary GWs. Thus, the fact that the wind perturbations are quite significant well above the

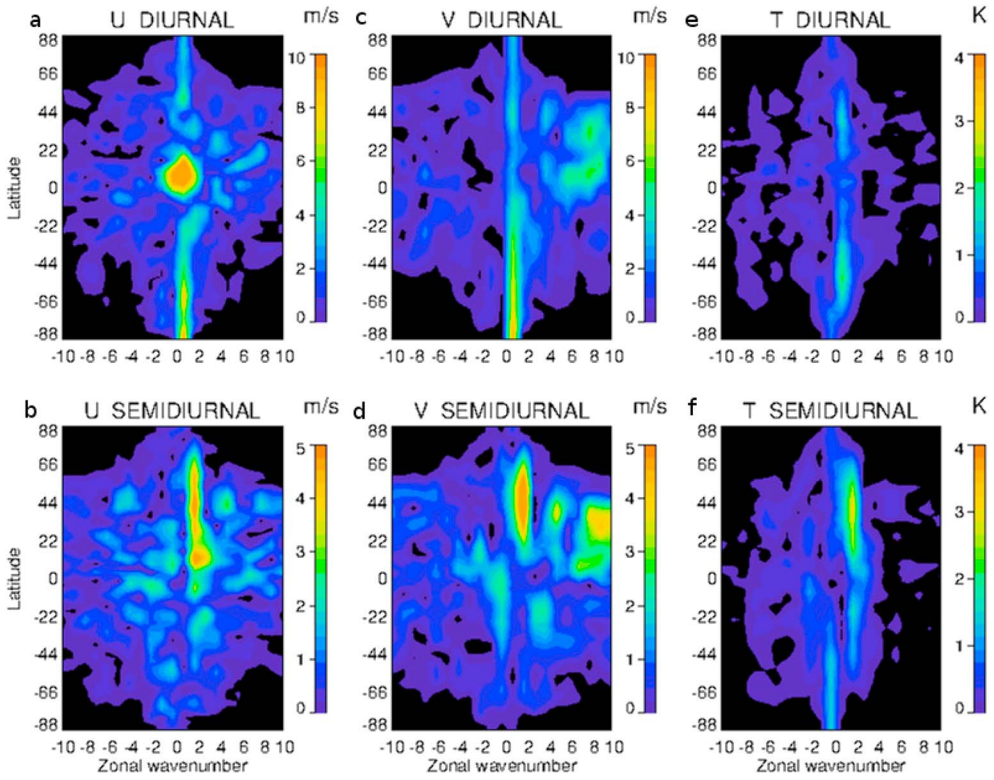

Figure 18. Planetary (a) diurnal and (b) semidiurnal amplitudes (in m/s) for u' from the TIME-GCM (gwfuvt-nogwf) on 17 June 2009 at $z = 250$ km as a function of latitude (y axis). Horizontal wave numbers −10 through 10 are shown on the x axis, with positive (negative) wave numbers denoting westward (eastward) wave propagation. (c, d) Same as Figures 18a and 18b but for the meridional velocity perturbation amplitude, v' (in m/s). (e, f) Same as Figures 18a and 18b but for the temperature perturbation amplitude, T' (in K).

force/heating altitude occurs because the secondary GW amplitudes grow exponentially with altitude (due to the decreasing background neutral density) while simultaneously decaying with altitude (due to molecular viscosity). The fact that there is little change in the wind perturbations with altitude occurs because the molecular viscosity smooths out the vertical structure of the perturbations and removes secondary GWs with smaller λ_z [*Vadas*, 2007].

Figure 12 shows the analogous result in 2000. Regions of large horizontal wind perturbations are apparent. These regions are highly correlated with significant regions of deep convection. Whereas u'_H tends to form clockwise and counterclockwise motions in 2009, they tend to form "jet"-like structures in 2000. We note that reasonably strong horizontal wind perturbations are created at $z = 150$–200 km with amplitudes that are ∼30% weaker than during 2009. However, whereas the horizontal wind perturbations only decrease slightly in altitude during 2009, they decrease substantially with altitude during 2000, reaching 1/2 of their magnitude by $z \sim 400$ km. This appears to be associated with the horizontal wind perturbations consisting mainly of large-scale secondary GWs with large λ_z during 2009 (identified by the circular motions in Figure 11), whereas they consist mainly of mean jet-like motions during 2000 (which are concentrated in altitude near the body forces that create them).

We examined the results at the altitudes $z = 150$, 200, and 250 km every 3 h over the 13 day study periods (i.e., at 00, 03 06 09, 12, 15, 18 and 21 UT). In 2009, we find that the global maximum (pinpoint) horizontal wind perturbations (at these altitudes every 3 h) are $\max(u'_H) \sim 30$–270 m/s and the average maximum (pinpoint) values are $\overline{\max(u'_H)} \sim 80$–$100$ m/s. In 2000, we find that the global maximum (pinpoint) horizontal wind perturbations (at these altitudes every 3 h) are $\max(u'_H) \sim 10$–190 m/s and the average maximum (pinpoint) values are $\overline{\max(u'_H)} \sim 30$–$50$ m/s.

While it is difficult to measure the neutral winds at $z \sim 150 - 200$ km, the neutral winds at $z \sim 250$ km can be obtained from the Fabry-Perot 630 nm emissions [e.g., *Makela et al.*, 2011]. However, these winds are

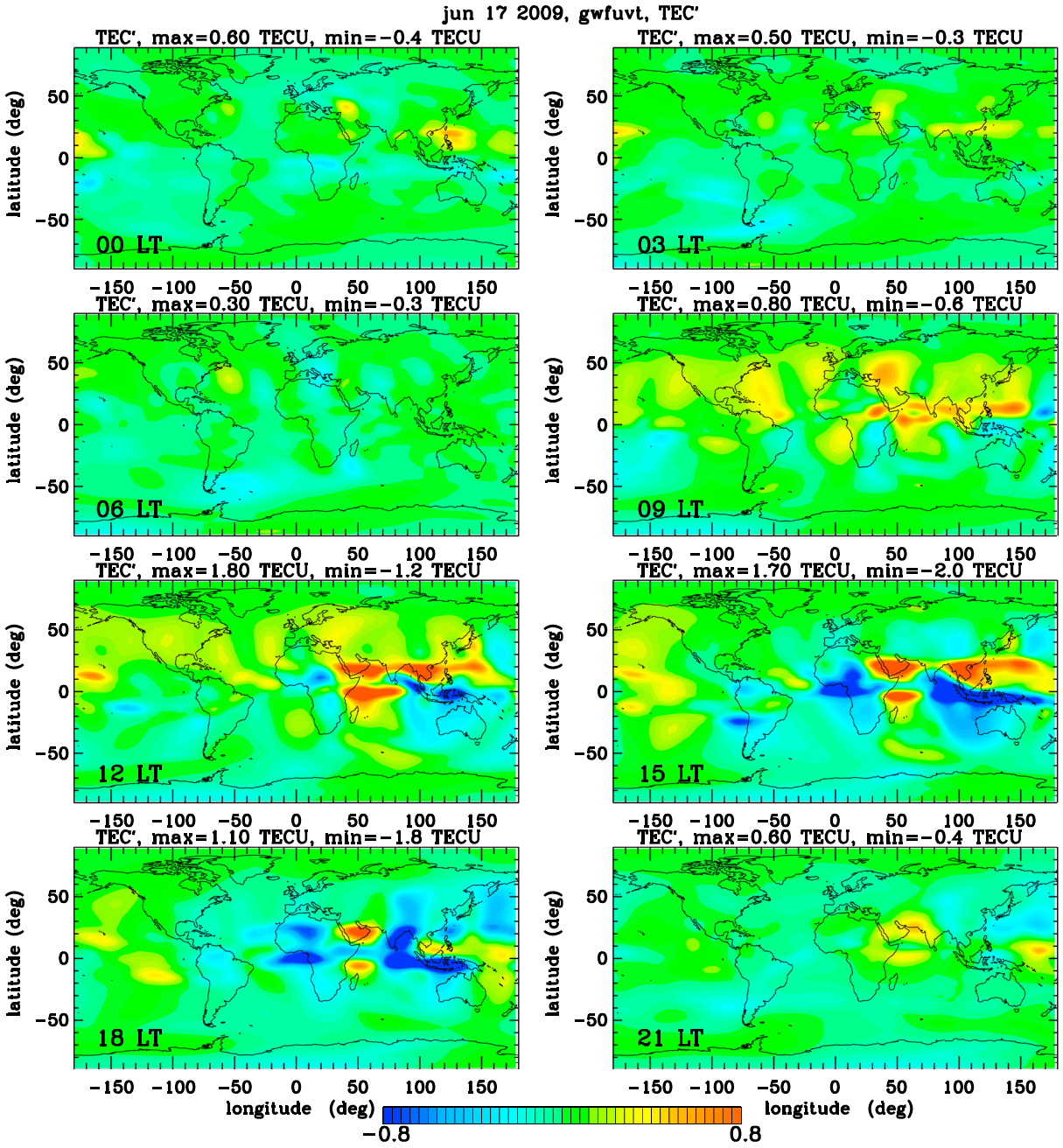

Figure 19. The TEC perturbation from the TIME-GCM, TEC′ (gwfuvt-nogwf), on 17 June 2009 every 3 h in local time (LT), as labeled. TEC′ is shown from blue (−0.8 TECU (total electron content unit, 1 TECU = 10^{16} el m^{-2})) to red (+0.8 TECU) in intervals of 0.04 TECU. The maximum and minimum values of TEC′ are listed at the top of each panel.

obtained by temporal averaging, and the 630 nm emission occurs over the altitude range $z \sim$ 220–280km. Both effects are expected to decrease the amplitudes of secondary wind perturbations to some degree. Additionally, our model results show that the largest horizontal wind perturbations occur within ±10° of the equator (and often over an ocean); thus, Fabry-Perot instruments would need to be strategically located to capture the wind perturbations modeled here. Finally, the force/heatings which lead to these large wind perturbations are located over regions of deep convection, where anvil clouds near the tropopause can obscure detection of the 630 nm emissions. All of these effects can decrease the measured wind perturbation amplitudes as compared to the actual values. Therefore, one must take appropriate care when comparing these model results with Fabry-Perot wind measurements.

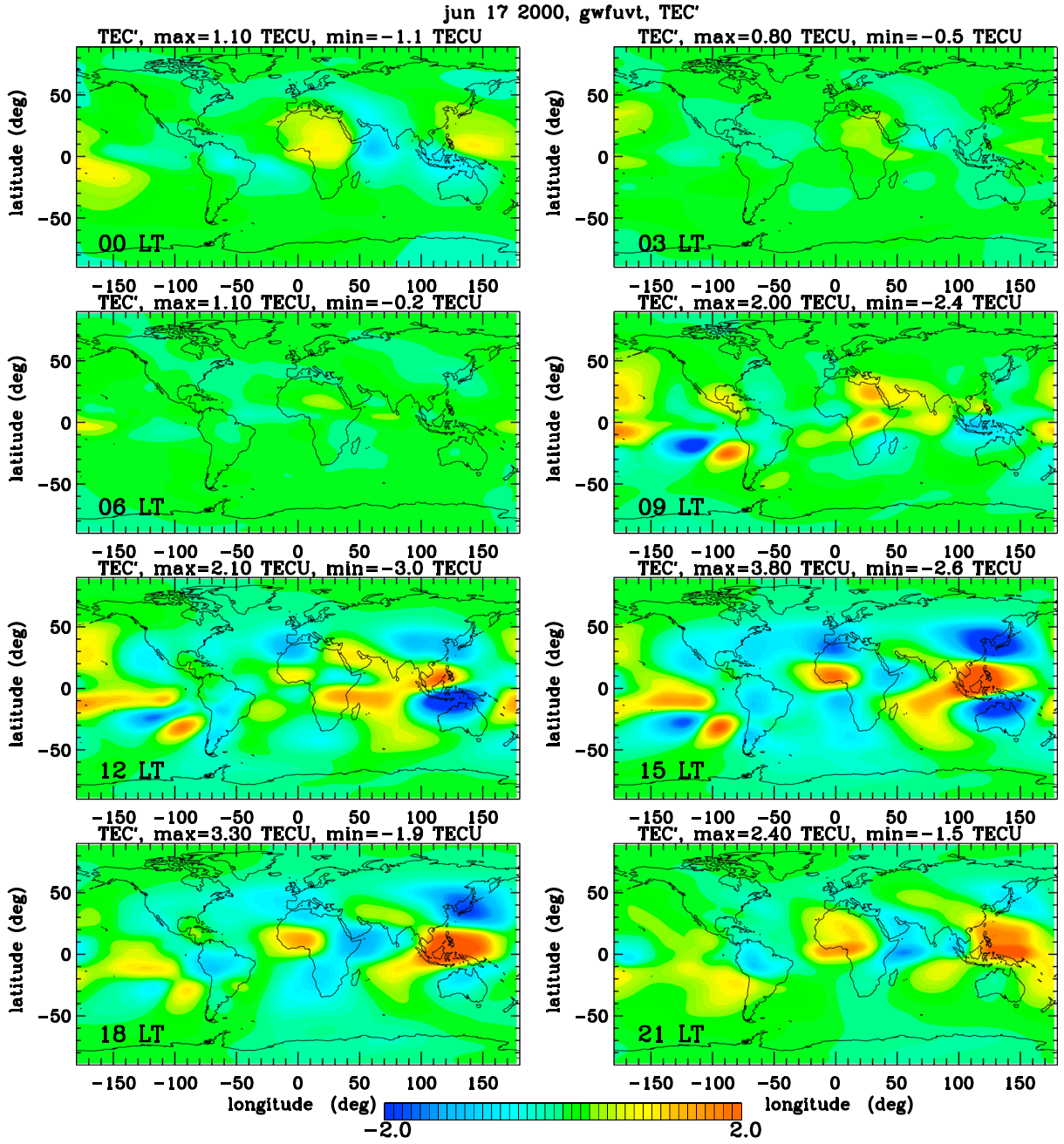

Figure 20. Same as Figure 19 but for 2000. TEC′ is shown from blue (−2 TECU) to red (+2 TECU) in intervals of 0.1 TECU.

4.2.4. Westward Propagation of the Temperature and Wind Perturbations

Figure 13 shows the evolution of T' (gwfuvt-nogwf) every 3 h on 17 June 2009 at $z = 350$ km. The induced temperature perturbations appear to propagate westward throughout the day, with a westward speed of ~ 460 m/s. Although the global distribution is complicated, one of the components has a period of 12 h and has two peaks in longitude (for a fixed UT). This structure and westward motion is clearly visible in Movie S1 in the supporting information.

The westward propagating two-peaked structure seen in Figure 13 is reminiscent of the migrating semidiurnal tide. The wind associated with this tide makes up a large component of the background horizontal wind at $z = 110$–200 km. As is well known, horizontal winds filter the GWs by changing their λ_z and intrinsic phase speeds, which in turn changes the altitudes where they dissipate [*Fritts and Vadas*, 2008].

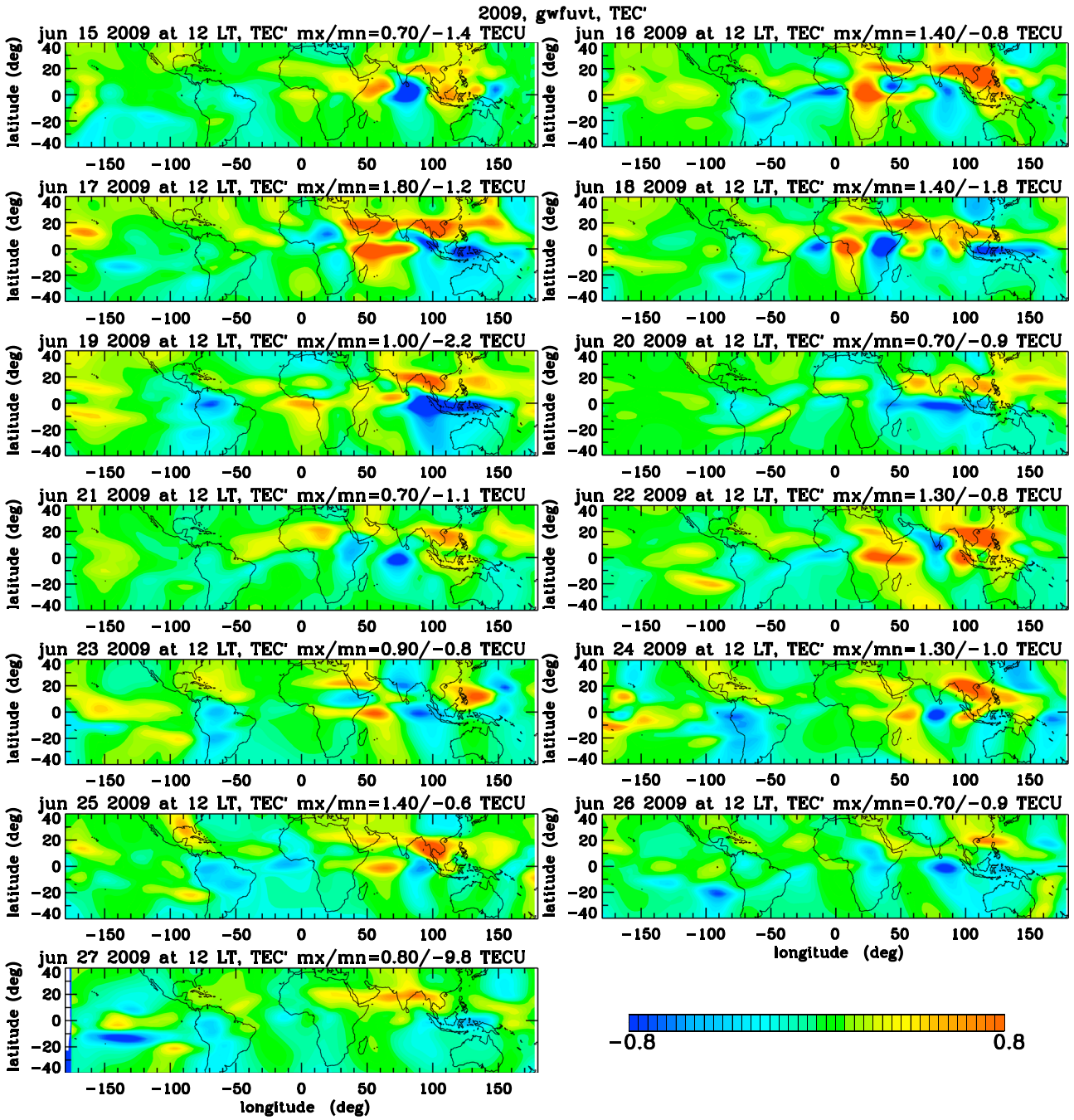

Figure 21. The TEC perturbation from the TIME-GCM, TEC′ (gwfuvt-nogwf), on 15–27 June 2009 at 12:00 LT. TEC′ is shown from blue (−0.8 TECU) to red (+0.8 TECU) in intervals of 0.04 TECU. The maximum and minimum values of TEC′ are listed at the top of each panel.

Vadas and Liu [2009] found that the wind most important for dissipative filtering occurs 1–2 neutral density scale heights below the altitude where the body force is maximum and that this maximum altitude occurs at $z \sim$170–200 km. In Figure 14, we show the total background wind at $z = 150$ km from the nogwf TIME-GCM on the same day and times. Although the wind is a complicated mix of many tides, the two-peaked, westward moving semidiurnal tide is visible.

Finally, we note that the zonal component of the wind at the equator is mostly westward in Figure 14. Such westward background winds enhance the propagation of eastward propagating GWs [*Fritts and Vadas*, 2008], thereby leading to an enhancement of the eastward body forces at $z \sim$ 170–200 km near

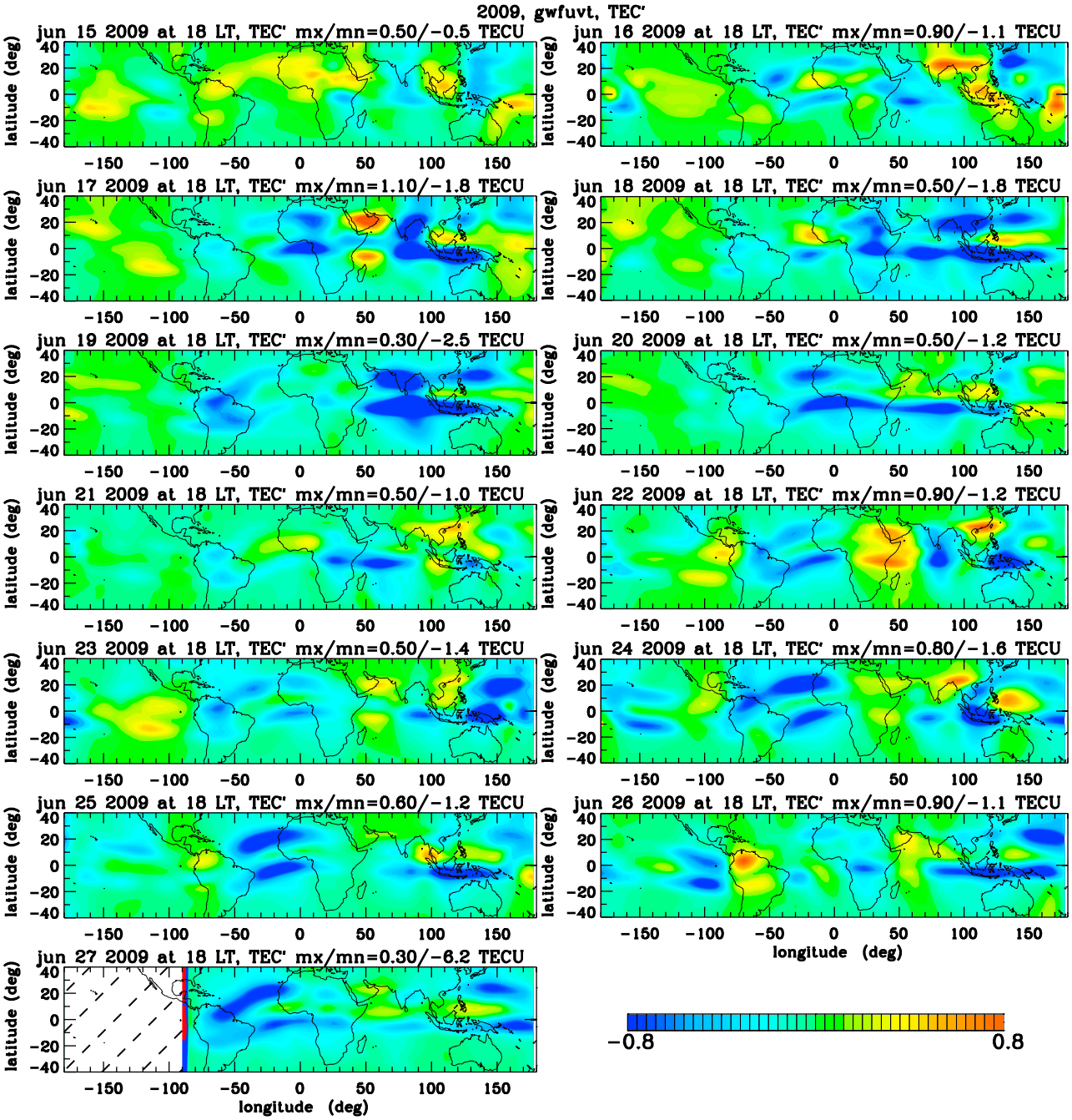

Figure 22. Same as Figure 21 but at 18:00 LT. The hatched region on 27 June denotes those locations where the universal time is greater than 0 UT on 28 June for this given LT.

the equator. This explains the enhancement of eastward wind perturbations created near the equator in Figure 9.

Figure 15 shows the horizontal velocity perturbations at $z = 200$ km on the same day and times as in Figure 13. Most of u'_H is highly correlated with regions of deep convection (e.g., Africa and Indian Ocean). This leads to variability on time scales of 3–6 h. Additionally, there is a small component of u'_H (with an amplitude of ~10–25 m/s) that propagates westward. This component may be associated with the westward moving semidiurnal tide identified earlier. This westward propagation can be seen in Movie S2 in the supporting information.

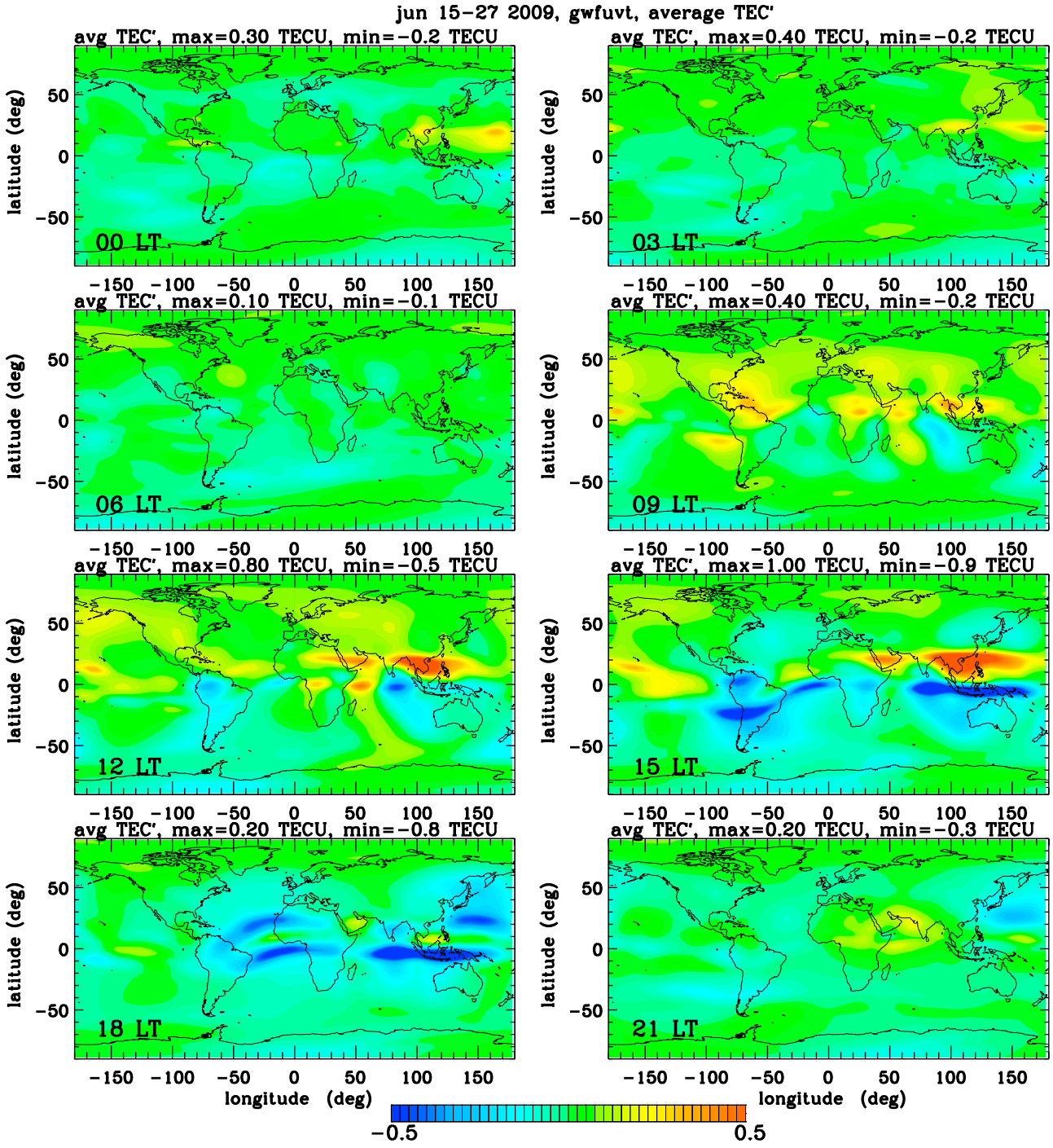

Figure 23. The average TEC perturbations from the TIME-GCM, $\overline{\text{TEC}'}$ (gwfuvt-nogwf) at 0, 3, 6, 9, 12, 15, 18, and 21 LT. For each LT, the average is taken from 15–27 June 2009. $\overline{\text{TEC}'}$ is shown from blue (−0.5 TECU) to red (+0.5 TECU) in intervals of 0.025 TECU. The maximum and minimum values of $\overline{\text{TEC}'}$ are listed at the top of each panel.

Figure 16 shows the evolution of T' every 3 h on 17 June 2000. Similar to Figure 13, the induced temperature perturbations propagate westward throughout the day. This is because the semidiurnal tide is one of the main components of the background (nogwf) horizontal winds at $z \sim 150$ km in 2000 (not shown). Additionally, similar to year 2009, the zonal component of the background wind at the equator is mostly westward at this altitude. This leads to the enhancement of eastward propagating GWs, which

leads to an enhancement of eastward body forces, which in turn leads to an enhancement of eastward wind perturbations at $z \sim 200$ km (e.g., Figure 9).

4.2.5. In Situ Generation of Planetary-Scale Tides

We now determine the planetary-scale components of the perturbations. (As before, these perturbations are calculated by subtracting the TIME-GCM solutions without the force/heatings from the TIME-GCM solutions with the force/heatings (gwfuvt-nogwf).) Because these perturbations are created by the dissipation (in the thermosphere) of the primary convectively generated GWs, these tidal components are generated "in situ" in the thermosphere at $z \sim 150$–280 km (where the body force/heatings are located). Perhaps one of the most likely creation mechanisms for the generation of these in situ tides is the filtering of GWs by tides (migrating and nonmigrating) in the mesosphere and lower thermosphere. (Note that migrating and nonmigrating tides are inputted into the TIME-GCM at the lower boundary via the GSWM-02 model (see section 4.1)). This would impart zonally averaged and planetary-scale variability at tidal periods to the body force/heatings, which would in turn excite in situ tidal components.

The global diurnal and semidiurnal in situ zonal winds are dominated by planetary-scale components. Figure 17 shows the diurnal and semidiurnal zonal wind perturbations, u', at $z = 250$ km on 17 June 2009, synthesized from the zonal mean and 10 eastward and westward traveling waves. The diurnal amplitudes are as large as ~40 m/s, while the semidiurnal amplitudes are as large as ~20 m/s. Thus, the diurnal wave amplitudes are a factor of 2 larger than the semidiurnal wave amplitudes.

Figure 18 shows the perturbation amplitudes of the diurnal and semidiurnal u', v', and T' as a function of zonal wavenumber and latitude. Positive (negative) wavenumbers denote westward (eastward) wave propagation. The leading diurnal component is the migrating tide (DW1), which travels westward with a zonal wave number 1. This wave has an amplitude of $u' \sim 13$ m/s near the equator and is responsible for the westward migration of the eastward wind maximum centered on the equator. The most significant additional diurnal u' components are the longitudinal mean ($s = 0$ or D0) and the westward propagating wave number 2 (DW2). These components have amplitudes of u'~10.5 m/s and 8.3 m/s, respectively. The meridional wind perturbation (v') shows additional westward traveling variability in wave numbers 5–9, with amplitudes of 5 m/s for each component.

The amplitude of the semidiurnal tide is about one half the amplitude of the diurnal tide. It is dominated by the migrating semidiurnal tide (a westward traveling zonal wave number 2 wave, or SW2), and westward traveling wave numbers 3 (SW3) in u' and 5 (SW5) in v'. These components all have amplitudes of ~5 m/s. Secondary maxima of ~3 m/s appear in v' at zonal wave numbers 0 (S0), eastward 2 (SE2), and SW3.

4.3. Large-Scale Changes to the Ionosphere

We now calculate the total electron content (TEC) by integrating vertical columns of the electron density from the TIME-GCM results. Because the TIME-GCM does not go above $z = 400$ or 500 km (depending on year, day, and time), this integration may not include all of the electrons in the ionosphere. We show the results in terms of the local time (LT), where we choose a simple, continuous definition of the LT:

$$\mathrm{LT} = \mathrm{UT} + \mathrm{longitude}/15. \tag{5}$$

Figure 19 shows the TEC perturbations, TEC′, created by GW dissipation every 3 h in local time on 17 June 2009. The TEC perturbations are concentrated near the equator and tend to be located near regions of deep convection (see Figure 3). They are largest during daytime hours when photoionization occurs. Figure 20 shows TEC′ on the same day in 2000. TEC′ is at least 2 times as large, mainly because there are more electrons due to a larger background density and stronger photoionization. Again, the TEC perturbations tend to be located near regions of deep convection (see Figure 6). From Figures 19 and 20, we see that there are typically two or three peaks in TEC′ around the Earth's circumference at the equator.

Figure 21 shows the TEC perturbations every day from 15 to 27 June 2009 at 12:00 LT. The perturbations are as large as 2.2 TECU (where TECU= 10^{16} el/m^2), and are strong in Africa, southern Asia, the Philippine Islands, and South America. The distributions change day to day, although there is often similarities for several days in a row (e.g., 16–18 June and 23–25 June). Figure 22 shows TEC′ every day during 2009 at 18:00 LT, which is 6 LT h later than Figure 21. At this time, the largest TEC perturbations are negative, with a maximum amplitude of 2.5 TECU, and tend to be concentrated in South America, the Atlantic Ocean, Africa, and the Philippines. Note that there tends to be two or three peaks in longitude around the Earth at the

equator. The fact that the TEC perturbations tend to be positive in Figure 21 and negative in Figure 22 suggests a semidiurnal component. This might be from semidiurnal wind filtering of the primary GWs in the lower thermosphere.

Figure 23 shows the average TEC′, $\overline{\text{TEC}'}$, every 3 h in local time. Here we average over the 13 day study period in 2009. $\overline{\text{TEC}'}$ depends strongly on the local time, with the largest values occurring at 15–18 LT. $\overline{\text{TEC}'}$ peaks at low equatorial latitudes. As before, there are typically two or three peaks in longitude.

5. Discussion and Conclusions

During the extreme solar minimum between solar cycles 23–24 (2007–2010), the Sun was extremely quiet, causing the temperature in the thermosphere to be quite low. We wished to understand how the dissipation of GWs excited by deep convection affected the large-scale dynamics of the thermosphere and ionosphere during this time. We chose the study period to be 15–27 June 2009, during the northern summertime. For comparison, we also choose the same study period during the previous solar maximum: 15–27 June 2000.

First, we identified all of the deep convective objects (plumes, clusters, and complexes) which overshot the tropopause throughout the Earth globally via the use of IR satellite images. We then modeled the primary GWs excited by these objects. We utilized a new global dissipative ray trace model and ray traced several millions GWs per object into the thermosphere, where they dissipated from viscosity and wave saturation. We then reconstructed the GW fields in the thermosphere and determined the body force/heat(cool)ings which resulted from GW dissipation. We then inputted these forces/heatings into the high-resolution TIME-GCM in order to determine the large-scale changes which occurred in the thermosphere and ionosphere.

We found that the body forces induced by the dissipation of primary GWs creates both wind (u'_H) and temperature (T') perturbations, while the heat(cool)ings induced by the dissipation of primary GWs create mainly temperature perturbations. We found that T' created by the body forces is $\sim$ 4–10 times larger than T' created by the heat/coolings. Typical maximum temperature perturbations were found to be ~10–40 K at $z \sim$ 150–250 km. The maximum heating amplitudes (ranging over all latitudes, longitudes and altitudes) during solar minimum had typical values of $\sim$ 0.003–0.07 K/s, with occasional values as large as ~0.1 K/s. The maximum heating amplitudes during solar maximum had typical values of ~0.002–0.05 K/s, with occasional values as large as $\sim$ 0.1–0.3 K/s.

As expected, we found that the body force amplitudes are ~2–3 times larger during solar minimum (2009) than during solar maximum (2000). This is because the background density decreases more rapidly with altitude during solar minimum, causing the kinematic viscosity to steepen more rapidly with altitude during solar minimum. The more rapid increase during solar minimum essentially acts like a viscous wall for GWs attempting to propagate to higher altitudes in the thermosphere. This causes the primary convective GWs to dissipate within a much smaller altitude range, thereby increasing the vertical divergence of the GW momentum flux. This results in much larger body force amplitudes during solar minimum than during solar maximum. The maximum horizontal body force amplitudes (ranging over all latitudes, longitudes, and altitudes) during solar minimum vary strongly with UT, with typical values of $\sim$ 0.08–0.5 m/s^2 and occasional values as large as $\sim$ 0.7–0.9 m/s^2. The maximum horizontal body force amplitudes during solar maximum have typical values of $\sim$ 0.03–0.2 m/s^2, occasional values as large as $\sim$ 0.3–0.5 m/s^2, and very rare values as large as $\sim$ 1.0 m/s^2 (primarily in the meridional direction). Because the body forces drive the horizontal wind perturbations, u'_H is proportional to the body force amplitudes. Therefore, the larger body forces also result in larger horizontal wind perturbations during solar minimum.

During both 2009 and 2000, we found that u'_H at z = 200 to 400 km is highly correlated with deep convective plumes overshooting the tropopause. During 2009, the u'_H motions generally exhibit clockwise and counterclockwise circulations, with spatial extents for the circulation cell pairs of 1000–5000 km. During 2000, although some circulations are seen, u'_H consists primarily of linear jet-like winds. At $z \sim$ 150–250 km, we found that the maximum (pinpoint) horizontal wind perturbations are max(u'_H) $\sim$ 30–270 m/s with an average maximum (pinpoint) value of $\overline{\max(u'_H)} \sim$ 80–100 m/s in 2009. For the same altitudes in 2000, the maximum (pinpoint) horizontal wind perturbations are max(u'_H) $\sim$ 10–190 m/s with an average maximum (pinpoint) value of $\overline{\max(u'_H)} \sim$ 30–50 m/s. These wind perturbations were found to persist to at least $z \sim$ 400 km, although with more of a reduction in altitude in 2000. Note that average values of u'_H at

$z = 400$ km were found to be similar to that of the background wind near the equator. Thus, our model results suggest that GW dissipation significantly affects the wind at $z \sim 200$–400 km at equatorial latitudes.

We then examined how T' evolved in time at $z = 350$ km. We found that T' appeared to be mainly westward moving, with a speed of ~ 460 m/s. One of the most obvious waves had two peaks in longitude and a 12 h period, characteristic of the migrating semidiurnal tide. We performed a planetary-scale analysis of u', v', and T', and found that in situ diurnal and semidiurnal tides were created in the thermosphere from the body force/heatings, likely due to imprinting of the primary GWs (and subsequently the body force/heatings) from tidal wind filtering in the lower thermosphere. We found that the diurnal tidal amplitudes at $z = 250$ km were as large as $u' \sim 40$ m/s, while the semidiurnal tidal amplitudes were as large as $u' \sim 20$ m/s. The largest-amplitude in situ tides were found to be DW1, D0, DW2, SW2, SW3, and SW5. Smaller-amplitude in situ tides were found to be S0, SE2, and SW3.

Finally, we calculated the total electron content perturbations (TEC′). We found that TEC′ are concentrated near the equator and tend to be located near regions of deep convection. During 2009 (2000), the TEC′ magnitudes are as large as ∼1–2.5 (∼2–3.5) TECU. The regions of largest TEC′ tend to occur midday to early evening. The TEC perturbations in 2009 have smaller amplitudes of ∼0.3–0.5 TECU during the late evening and early morning hours. Because the perturbations tend to be positive (negative) at 12 LT (18 LT), there appears to be a semidiurnal periodicity in TEC′, likely created by the semidiurnal periodicity of the force/heatings (due to imprinting of the primary GWs via simidiurnal tidal wind filtering in the lower thermosphere). For a given LT, the spatial distribution of TEC′ tends to retain coherency over several days, reflective of the several day temporal coherency of the underlying deep convection. Finally, we find that the spatial distribution of the average TEC′ depends sensitively on the local time and peaks at low equatorial latitudes. For a given LT, there are typically two to three peaks in longitude around the Earth during the 2009 study period.

Acknowledgments

We would like to thank meteorologists Pete Stamus and Patrice Sutter for determining the parameters of the overshooting convective objects, Ben Foster for implementing the body forces into the TIME-GCM, and Wenbin Wang for reviewing the paper. S.L.V. was supported by NASA contract NNH10CC98C. H.L.L. was supported in part by NASA contract NNH10CC98C. The National Center for Atmospheric Research is sponsored by the National Science Foundation. We acknowledge and thank ECMWF/ERA-Interim for the use of their lower atmospheric meteorological data. We acknowledge and thank the NASA supercomputer center for the use of Pleiades to run our ray trace model. The data shown in this paper may be available for collaborative research pending an email request to the authors.

Alan Rodger thanks the reviewers for their assistance in evaluating this paper.

References

Alexander, M. J., J. R. Holton, and D. R. Durran (1995), The gravity wave response above deep convection in a squall line simulation, *J. Atmos. Sci.*, *52*(12), 2212–2226, doi:10.1175/1520-0469.

Araujo-Pradere, E. A., R. Redmon, M. Fedrizzi, R. Viereck, and T. J. Fuller-Rowell (2011), Some characteristics of the ionospheric behavior during the solar cycle 23–24 minimum, *Sol. Phys.*, *274*, 439–456, doi:10.1007/s11207-011-9728-3.

Becker, E. (2004), Direct heating rates associated with gravity wave saturation, *J. Atmos. Terr. Phys.*, *66*, 683–696.

Beres, J. H. (2004), Gravity wave generation by a three-dimensional thermal forcing, *J. Atmos. Sci.*, *61*, 1805–1815.

Bretherton, F. P. (1969), On the mean motion induced by internal gravity waves, *J. Fluid Mech.*, *36*, 785–803.

Chapagain, N. P., J. J. Makela, J. W. Meriwether, D. J. Fisher, R. A. Buriti, and A. F. Medeiros (2012), Comparison of nighttime zonal neutral winds and equatorial plasma bubble drift velocities over Brazil, *J. Geophys. Res.*, *117*, A06309, doi:10.1029/2012JA017620.

Choi, H.-J., H.-Y. Chun, and I.-S. Song (2007), Characteristics and momentum flux spectrum of convectively forced internal gravity waves in ensemble numerical simulations, *J. Atmos. Sci.*, *64*(10), 3723–3734.

Cotton, W. R., and R. A. Anthes (1989), *Storm and Cloud Dynamics*, 883 pp., Academic Press, San Diego, Calif.

DelGenio, A. D., and G. Schubert (1979), Gravity wave propagation in a diffusively separated atmosphere with height-dependent collision frequencies, *J. Geophys. Res.*, *84*, 4371–4378.

Eckermann, S., and C. Marks (1996), An idealized ray model of gravity wave-tidal interactions, *J. Geophys. Res.*, *101*(D16), 21,195–21,212, doi:10.1029/96JD01660.

Emmert, J. T., J. L. Lean, and J. M. Picone (2010), Record-low thermospheric density during the 2008 solar minimum, *Geophys. Res. Lett.*, *37*, L12102, doi:10.1029/2010GL043671.

Fritts, D. C., and M. J. Alexander (2003), Gravity wave dynamics and effects in the middle atmosphere, *Rev. Geophys.*, *41*(1), 1003, doi:10.1029/2001RG000106.

Fritts, D. C., and S. Vadas (2008), Gravity wave penetration into the thermosphere: Sensitivity to solar cycle variations and mean winds, *Ann. Geophys.*, *26*, 3841–3861, doi:10.5194/angeo-26-3841-2008.

Fritts, D. C., S. L. Vadas, and Y. Yamada (2002), An estimate of strong local body forcing and gravity wave radiation based on OH airglow and meteor radar observations, *Geophys. Res. Lett.*, *29*(10), 1429, doi:10.1029/2001GL013753.

Fritts, D. C., S. L. Vadas, K. Wan, and J. A. Werne (2006), Mean and variable forcing of the middle atmosphere by gravity waves, *J. Atmos. Sol. Terr. Phys.*, *68*, 247–265.

Graham, N. E, and T. P. Barnett (1987), Sea surface temperature, surface wind divergence, and convection over tropical oceans, *Science*, *238*(4827), 657–659, doi:10.1126/science.238.4827.657.

Gossard, E. E., and W. H. Hooke (1975), *Waves in the Atmosphere: Atmospheric Infrasound and Gravity Waves, Their Generation and Propagation*, 456 pp., Elsevier Science, Amsterdam, Netherlands.

Haaser, R. A., G. D. Earle, R. A. Heelis, W. R. Coley, and J. H. Klenzing (2010), Low-latitude measurements of neutral thermospheric helium dominance near 400 km during extreme solar minimum, *J. Geophys. Res.*, *115*, A11318, doi:10.1029/2010JA015325.

Hagan, M., and J. Forbes (2003), Migrating and nonmigrating semidiurnal tides in the upper atmosphere excited by tropospheric latent heat release, *J. Geophys. Res.*, *108*(A2), 1062, doi:10.1029/2002JA009466.

Hagan, M. E., and J. M. Forbes (2002), Migrating and nonmigrating diurnal tides in the middle and upper atmosphere excited by tropospheric latent heat release, *J. Geophys. Res.*, *107*(D24), 4754, doi:10.1029/2001JD001236.

Hecht, J. H., R. L. Walterscheid, D. C. Fritts, J. R. Isler, D. C. Senft, C. S. Gardner, and S. J. Franke (1997), Wave breaking signatures in OH airglow and sodium densities and temperatures. Part I: Airglow imaging, Na lidar, and MF radar observations, *J. Geophys. Res.*, *102*, 6655–6668.

Holton, J. R., and M. J. Alexander (1999), Gravity waves in the mesosphere generated by tropospheric convection, *Tellus*, *51A-B*, 45–58.

Horinouchi, T., T. Nakamura, and J.-I. Kosaka (2002), Convectively generated mesoscale gravity waves simulated throughout the middle atmosphere, *Geophys. Res. Lett.*, *29*(21), 2007, doi:10.1029/2002GL016069.

Lane, T. P., M. J. Reeder, and T. L. Clark (2001), Numerical modeling of gravity waves generated by deep tropical convection, *J. Atmos. Sci.*, *58*, 1249–1274.

Lane, T. P., R. D. Sharman, T. L. Clark, and H.-M. Hsu (2003), An investigation of turbulence generation mechanisms above deep convection, *J. Atmos. Sci.*, *60*, 1297–1321, doi:10.1175/1520-0469.

Larsen, M. F., and C. G. Fesen (2009), Accuracy issues of the existing thermospheric wind models: Can we rely on them in seeking solutions to wind-driven problems?, *Ann. Geophys.*, *27*, 2277–2284.

Lindzen, R. S. (1981), Turbulence and stress owing to gravity wave and tidal breakdown, *J. Geophys. Res.*, *86*(C10), 9707–9714.

Liu, H.-L. (2000), Temperature changes due to gravity wave saturation, *J. Geophys. Res.*, *105*(D10), 12,329–12,336, doi:10.1029/2000JD900054.

Liu, H.-L., and S. L. Vadas (2013), Large-scale ionospheric disturbances due to the dissipation of convectively-generated gravity waves over Brazil, *J. Geophys. Res. Space Physics*, *118*, 2419–2427, doi:10.1002/jgra.50244.

Lund, T. S., and D. C. Fritts (2012), Numerical simulation of gravity wave breaking in the lower thermosphere, *J. Geophys. Res.*, *117*, D21105, doi:10.1029/2012JD017536.

Makela, J. J., J. W. Meriwether, Y. Huang, and P. J. Sherwood (2011), Simulation and analysis of a multi-order imaging Fabry-Perot interferometer for the study of thermospheric winds and temperatures, *Appl. Opt.*, *50*, 4403–4416.

Miyoshi, Y., and H. Fujiwara (2008), Gravity waves in the thermosphere simulated by a general circulation model, *J. Geophys. Res.*, *113*, D01101, doi:10.1029/2007JD008874.

Nicolls, M. J., S. L. Vadas, J. W. Meriwether, M. G. Conde, and D. Hampton (2012), The phases and amplitudes of gravity waves propagating and dissipating in the thermosphere: Application to measurements over Alaska, *J. Geophys. Res.*, *117*, A05323, doi:10.1029/2012JA017542.

Pandya, R. E., and M. J. Alexander (1999), Linear stratospheric gravity waves above convective thermal forcing, *J. Atmos. Sci.*, *56*(14), 2434–2446.

Piani, C., D. Durran, M. J. Alexander, and J. R. Holton (2000), A numerical study of three dimensional gravity waves triggered by deep tropical convection, *J. Atmos. Sci.*, *57*, 3689–3702.

Roble, R. G., and E. C. Ridley (1994), A thermosphere-ionosphere-mesosphere-electrodynamics general circulation model (TIME-GCM): Equinox solar cycle minimum simulations (30–500km), *Geophys. Res. Lett.*, *21*, 417–420, doi:10.1029/93GL03391.

Song, I.-S., H.-Y. Chun, and P. P. Lane (2003), Generation mechanisms of convectively forced internal gravity waves and their propagation to the stratosphere, *J. Atmos. Sci.*, *60*, 1960–1980.

Stull, R. B. (1976), Internal gravity waves generated by penetrative convection, *J. Atmos. Sci.*, *33*(7), 1279–1286.

Vadas, S. L. (2007), Horizontal and vertical propagation and dissipation of gravity waves in the thermosphere from lower atmospheric and thermospheric sources, *J. Geophys. Res.*, *112*, A06305, doi:10.1029/2006JA011845.

Vadas, S. L. (2013), Compressible f-plane solutions to body forces, heatings, and coolings, and application to the primary and secondary gravity waves generated by a deep convective plume, *J. Geophys. Res. Space Physics*, *118*, 2377–2397, doi:10.1002/jgra.50163.

Vadas, S. L., and G. Crowley (2010), Sources of the traveling ionospheric disturbances observed by the ionospheric TIDDBIT sounder near Wallops Island on October 30, 2007, *J. Geophys. Res.*, *115*, A07324, doi:10.1029/2009JA015053.

Vadas, S. L, and D. C. Fritts (2004), Thermospheric responses to gravity waves arising from mesoscale convective complexes, *J. Atmos. Sol. Terr. Phys.*, *66*, 781–804.

Vadas, S. L., and D. C. Fritts (2005), Thermospheric responses to gravity waves: Influences of increasing viscosity and thermal diffusivity, *J. Geophys. Res.*, *110*, D15103, doi:10.1029/2004JD005574.

Vadas, S. L., and D. C. Fritts (2006), Influence of solar variability on gravity wave structure and dissipation in the thermosphere from tropospheric convection, *J. Geophys. Res.*, *111*, A10S12, doi:10.1029/2005JA011510.

Vadas, S. L., and D. C. Fritts (2009), Reconstruction of the gravity wave field from convective plumes via ray tracing, *Ann. Geophys.*, *27*, 147–177.

Vadas, S. L., and H.-L. Liu (2009), The generation of large-scale gravity waves and neutral winds in the thermosphere from the dissipation of convectively-generated gravity waves, *J. Geophys. Res.*, *114*, A10310, doi:10.1029/2009JA014108.

Vadas, S. L., and H.-L. Liu (2013), Numerical modeling of the large-scale neutral and plasma responses to the body forces created by the dissipation of gravity waves from 6 h of deep convection in Brazil, *J. Geophys. Res. Space Physics*, *118*, 2593–2617, doi:10.1002/jgra.50249.

Vadas, S. L., D. C. Fritts, and M. J. Alexander (2003), Mechanism for the generation of secondary waves in wave breaking regions, *J. Atmos. Sci.*, *60*, 194–214.

Vadas, S. L., J. Yue, C.-Y. She, P. A. Stamus, and A. Liu (2009), A model study of the effects of winds on concentric rings of gravity waves from a convective plume near Fort Collins on 11 May 2004, *J. Geophys. Res.*, *114*, D06103, doi:10.1029/2008JD010753.

Vadas, S. L., J. Yue, and T. Nakamura (2012), Mesospheric concentric gravity waves generated by multiple convection storms over the North American Great Plain, *J. Geophys. Res.*, *117*, D07113, doi:10.1029/2011JD017025.

Walterscheid, R. L. (1981), Dynamical cooling induced by dissipating internal gravity-waves, *J. Geophys. Res.*, *8*, 1235–1238.

Walterscheid, R. L., G. Schubert, and D. G. Brinkman (2001), Small-scale gravity waves in the upper mesosphere and lower thermosphere generated by deep tropical convection, *106*, *D23*, 31,825–31,832.

Yamada, Y., H. Fukunishi, T. Nakamura, and T. Tsuda (2001), Breaking of small-scale gravity wave and transition to turbulence observed in OH airglow, *Geophys. Res. Lett.*, *28*, 2153–2156.

Yiğit, E., and A. S. Medvedev (2009), Heating and cooling of the thermosphere by internal gravity waves, *Geophys. Res. Lett.*, *36*, L14807, doi:10.1029/2009GL038507.

Yiğit, E., A. S. Medvedev, A. D. Aylward, P. Hartogh, and M. J. Harris (2009), Modeling the effects of gravity wave momentum deposition on the general circulation above the turbopause, *J. Geophys. Res.*, *114*, D07101, doi:10.1029/2008JD011132.